Engineering Structures 219 (2020) 110896

Contents lists available at ScienceDirect

Engineering Structures

journal homepage: www.elsevier.com/locate/engstruct

Composite behavior in RC buildings retrofitted using buckling-restrained braces with elastic steel frames

Panumas Saingam[a], Fatih Sutcu[b], Yuki Terazawa[a], Kazuhiro Fujishita[c], Pao-Chun Lin[a], Oguz C. Celik[d], Toru Takeuchi[a,*]

[a] Department of Architecture and Building Engineering, Tokyo Institute of Technology, Tokyo, Japan
[b] Faculty of Civil Engineering, Istanbul Technical University, Istanbul, Turkey
[c] Kozo Keikaku Engineering, Tokyo, Japan
[d] Structural & Earthquake Engineering Division, Faculty of Architecture, Istanbul Technical University, Istanbul, Turkey

ARTICLE INFO

Keywords:
Seismic retrofit
RC buildings
Buckling-restrained braces
Composite behavior
Equivalent linearization

ABSTRACT

Seismically retrofitting reinforced concrete (RC) building with a combination of buckling-restrained braces (BRBs) and elastic steel frames offers a practical solution that provides additional lateral stiffness and energy dissipation capacity. However, the available methods to vertically distribute the BRB sizes based on equivalent linearization do not consider the additional stiffness due to the composite behavior between the RC frame and the elastic steel frame, which may lead to an overly conservative estimate of the BRB stiffness demands. This study proposes a retrofit design method incorporating the composite behavior. Numerical models considering the detailed composite behavior are developed and calibrated against quasi-static cyclic loading tests, and a simplified evaluation method is proposed. A four-story RC school building is used as a benchmark model, and the proposed retrofit design method is validated using nonlinear response history analysis. The analysis results suggest that taking the composite behavior into account by using the proposed retrofit design method more accurately estimates the lateral stiffness of the retrofitted structure and leads to a more economic retrofit.

1. Introduction

Post-earthquake investigations have found damage in many older RC buildings due to insufficient lateral force resisting systems. For example, extensive damage was observed in RC buildings during the January 17th, 1994 Northridge Earthquake in the USA [1], the January 17th, 1995, Kobe (Great Hanshin) Earthquake in Japan [2], the September 21st, 1999 Chi-Chi Earthquake in Taiwan [3], the May 5th, 2014 Mae Lao Earthquake in Thailand [4], the 1999 Kocaeli earthquake in Turkey [5], and the central Italy Earthquakes in 2016 [6]. This highlights the need to develop strategies to retrofit older sub-standard RC buildings.

The decision between rebuilding or retrofitting a structure depends on the total construction cost, construction time, and intended post-earthquake performance objective, which is described in FEMA P-58 [7]. The adopted performance objective may be evaluated from the expected economic losses and downtime [8], and is developed for existing school buildings in the retrofit guideline in [9]. Based on these guidelines, demolishing seismically vulnerable existing buildings and replacing with new construction is an option, but is often time-consuming and expensive. In addition, rebuilding imposes other costs when the number of schools or hospitals is limited in a rural area, as there may be limited alternative facilities to conduct the education or medical functions. Therefore, there is a need to retrofit old RC buildings that were either not originally designed for seismic effects or were designed to an outdated seismic specification. To this end, updated seismic design specifications are usually referred for retrofit design to ensure that the retrofitted RC building is capable of resisting future earthquakes.

Methods commonly used to retrofit RC buildings by increasing the lateral force capacity include adding RC walls [10–11], wrapping the RC columns with carbon fiber reinforced polymers [12–15], adding self-centering braces [16–20], and adding conventional steel braces [21–27]. However, the study in [28] found that conventional retrofitting schemes that strengthen or stiffen the structure by jacketing the columns and beam-column joints or adding RC walls might actually lead to worse building performance in terms of the expected annual loss (EAL) ratio. This is mainly from the combined effect of an increase in damage due to higher maximum floor accelerations and a shift in the mean hazard curve due to period shortening. The primary benefits of

* Corresponding author.
E-mail address: takeuchi.t.ab@m.titech.ac.jp (T. Takeuchi).

https://doi.org/10.1016/j.engstruct.2020.110896
Received 14 January 2020; Received in revised form 19 May 2020; Accepted 28 May 2020
Available online 22 June 2020
0141-0296/

Nomenclature

A_a	Cross-section area of a RC post-installed anchor
A_e	Cross-section area of BRB elastic segment
A_m	Contact area between mortar block and RC frame
A_{max}	Maximum roof acceleration
A_p	Cross-section area of BRB plastic segment
E	Elastic modulus of the BRB steel core
E_a	Elastic modulus of a RC post-installed anchor
E_d	Energy dissipated by the BRB
E_I	Total input energy
E_m	Elastic modulus of the mortar block
$(EI)_{cb,p}$	Flexural rigidity of the RC beam, deforming in positive bending
$(EI)_{cb,n}$	Flexural rigidity of the RC beam, deforming in negative bending
$(EI)_{cc,l}$	Flexural rigidity of the left RC column
$(EI)_{cc,r}$	Flexural rigidity of the right RC column
$(EI)_{eqb,p}$	Equivalent flexural rigidity of the RC beam with adjacent SF in positive bending
$(EI)_{eqb,n}$	Equivalent flexural rigidity of the RC beam with adjacent SF in negative bending
$(EI)_{eqc,l}$	Equivalent flexural rigidity of the left RC column with adjacent SF
$(EI)_{eqc,r}$	Equivalent flexural rigidity of the right RC column with adjacent SF
$(EI)_{SFb}$	Flexural rigidity of the steel frame (SF) beam
$(EI)_{SFc,l}$	Flexural rigidity of the left steel frame (SF) column
$(EI)_{SFc,r}$	Flexural rigidity of the right steel frame (SF) column
F_C	Compression capacity of the MLP link
F_T	Tension capacity of the MLP link
G_m	Shear modulus of mortar
h_{eq}	Equivalent damping ratio
H_{eq}	Equivalent height of the $SDOF_{RC}$ model
H_{Ieq}	Distance between the neutral axes of the top and bottom composite beams for a given story
K_{BRB}	Axial BRB work-point stiffness
K_C	Compressive stiffness of the mortar block
K_d	Lateral story stiffness of BRB
$K_{d,i}$	Required lateral BRB stiffness at i^{th} story, neglecting RC frame and SF composite behavior
$K_{dc,i}$	Required lateral BRB stiffness at i^{th} story, considering RC frame and SF composite behavior
K_{Ieq}	Stiffness of the retrofitted structure with fully composite RC frame and SF connection
$K_{f,i}$	Story stiffness of existing RC building at i^{th} story, obtained by pushover analysis
K_f	Lateral stiffness of the $SDOF_{RC}$ model
$K_{f,l}$	Lateral stiffness of the $SDOF_{RC}$ model in the longitudinal direction
$K_{f,t}$	Lateral stiffness of the $SDOF_{RC}$ model in the transverse direction
$K_{R,i}$	Lateral stiffness of the i^{th} story of the retrofitted building with BRBs and SFs, considering composite behavior
K_{RC}	Lateral stiffness of RC frame within the retrofit bay
K_{RS}	Lateral stiffness of building retrofitted with the SF only, considering composite behavior
K_s	Shear stiffness of the MLP link
K_{SF}	Lateral stiffness of steel frame (SF)
K_T	Tension stiffness of the MLP link
l_{Ieq}	Distance between the neutral axes of the left and right composite columns
L_a	Effective length equivalent to half of the anchor embedded length
L_{BRB}	Work-point length of the BRB
L_e	Length of each BRB elastic segment
L_m	Length of the mortar block in contact with the RC frame
L_p	Length of BRB plastic segments
M	Bending moment of RC column
M_{eq}	Equivalent mass of the $SDOF_{RC}$ model
N_y	Axial yield force capacity of the BRB
P	Axial force of RC column
Q_{a1}	Shear strength of MLP link, determined by steel strength of anchor
Q_{a2}	Shear strength of MLP link, determined by bearing strength of concrete against anchor
R_E	Ratio of hysteretic energy dissipated by BRBs (E_d) to the total input energy (E_I)
S_{DS}	Design spectral acceleration at 0.2 sec
S_{D1}	Design spectral acceleration at 1.0 sec
T_{eq}	Equivalent secant period
δ_{dy}	Lateral yield deformation of the BRB
$\delta_{dy,\theta}$	Axial yield deformation of the BRB
$\delta_{d,l}$	Spectral displacement of the $SDOF_{RC}$ model in the longitudinal direction
$\delta_{d,t}$	Spectral displacement of the $SDOF_{RC}$ model in the transverse direction
δ_{fy}	Lateral yield deformation of the $SDOF_{RC}$
δ_r	Reduced spectral displacement
W_{BRB}	Weight of the BRB steel
θ_{BRB}	Inclination angle of BRB
ε_y	Yield strain of the BRB steel core
μ_d	Displacement ductility ratio of BRB
μ_f	Displacement ductility of the $SDOF_{RC}$ model
σ_a	Yield stress of the anchor material
σ_c	Compressive strength of the concrete
$\gamma_{cf,i}$	Fully composite stiffness amplification ratio at i^{th} story, expressing the fully composite stiffness relative to the non-composite stiffness of the RC frame and SF
$\gamma_{cp,i}$	Partially composite stiffness amplification ratio at i^{th} story, expressing the actual composite stiffness obtained from pushover analysis relative to the non-composite stiffness of the RC frame and SF

these retrofit strategies are a reduction in the maximum story drift and preventing a soft-story collapse. Therefore, these conventional schemes reduce drift-induced damage while increasing acceleration-induced damage, which may nevertheless leave the building inoperative due to excessive nonstructural (i.e. architectural) damage. Similar observations have been made for strengthening and stiffening masonry infill panels using fiber reinforcing polymer wraps [29,30], which may be less sustainable from an economic point of view as compared to other techniques such as base isolation. These studies found that the FRP wrapping did not improve the EAL to a significant degree compared to the initial cost of retrofitting. The above remarks regarding the trade-off in drift and acceleration-related damage when strengthening and stiffening the structures play a significant role when assessing the effectiveness of a seismic retrofit.

Steel braced frame systems have proven advantageous for retrofit [16–27] as steel braces may be prefabricated and are lighter than structural RC walls. When retrofitting RC buildings, limiting the maximum inter-story drift is important in preventing structural and nonstructural damage, and steel braces are effective in increasing the stiffness and reducing drifts. However, increasing the lateral stiffness amplifies the response accelerations, the same problem encountered when retrofitting with RC walls. In addition, steel braces buckle in compression, which may result in unsymmetrical lateral stiffness of the overall system. Buckling-restrained brace (BRB) may be a useful seismic retrofit device, as global buckling of the axially yielding steel core is suppressed by an axially decoupled restraining mechanism [31,32]. Retrofitting of RC buildings with BRBs offers an alternative for bracing retrofit as the BRB develops full yield strength both in tension and compression through its buckling preventing mechanism [33–44]. This enables BRBs to dissipate energy even during large earthquakes (such as the MCE level). It was shown in [44] that, when properly designed, RC frames retrofitted with a combination of BRBs and elastic steel frames would achieve the desired response by controlling inelastic demands (e.g. cracks, steel rebar strains) in the existing RC elements while providing the required strength, stiffness, and ductility. Therefore, in the RC building retrofit, the inter-story drift response can be reduced by the additional stiffness of the BRBs, while the enhanced energy dissipation helps mitigate the adverse effect of the additional stiffness on the response accelerations.

Directly installing either conventional concentric braces or BRBs in RC frames is often not practical when the axial force capacities of the braces are large. The brace connection details generally increase the demands on the original RC connections [45–46], and may induce additional axial forces, particularly in the lower story columns. However, installing an elastic steel frame (SF) between the RC frame and BRB (Fig. 1) offers a practical solution [41–44], as the SF avoids force concentration at the beam-to-column joint that results from the axial force induced by the BRB. In addition, the SF provides an interface that enables easier installation of the BRB into the RC frame compared to a pure gusset detailing. The SF is designed to remain elastic to provide a restoring force in order to reduce residual story drift after earthquakes. A parametric study covering a range of SF sections [41] concluded that when the SF lateral stiffness is approximately 5% of the BRB lateral stiffness, the residual story drift could be efficiently reduced because of the elastic SF's self-centering function. As shown in Fig. 1, the SF members may be attached to the RC frame using chemical anchors post-installed to the RC frame and steel studs welded on the SF members. High strength mortar is used as an infill material within this connection zone. This connection zone between the RC frame and the SF introduces a composite behavior, which increases the combined lateral stiffness of the retrofitted building. Note that this results in a greater combined lateral stiffness than the RC frame and SF acting independently.

The dynamic characteristics of a retrofitted RC building with BRBs and SFs may be significantly altered due to the increased lateral stiffness. Therefore, the seismic demand must be updated to account for the increased stiffness, which increases the complexity and time it takes to design the BRBs and the SF member. One approach is to simplify the structure into a single-degree-of-freedom (SDOF) model [41–43] that represents the seismically retrofitted RC building with BRBs and SFs, and then apply the equivalent linearization approach [47]. Here, the required stiffness of the BRB and SF are calculated from the SDOF model. If the retrofitted story drifts at each story are identical to the simplified SDOF model, an ideal uniform story drift distribution along the building height may be achieved [41–42]. These studies [41–42] proposed a retrofit design method that avoids the need for iteration when designing the BRBs and SF members for a target deformation. This procedure is referred to as the constant drift (CD) method. However, the previously proposed CD method does not consider the composite behavior between the RC frame and SF, as the lateral stiffness of the retrofit structure is calculated by simply adding the stiffness of the RC frame, SF, and BRB together. As a result, the required BRB stiffness may be overdesigned as the effective lateral stiffness of the combined RC frame and SF is underestimated by not taking the composite behavior into account.

This study investigates the influence of the composite behavior between the RC frame and SF on the retrofitted RC building by using experimentally calibrated numerical models, in order to achieve more economic and reliable results. The axial and shear-deformation relationships are proposed and validated against a near full-scale quasi-static cyclic loading test of a single-story retrofitted RC building [44]. The complicated connection zone between the RC frame and SF is modeled using link elements. Amplification ratios are proposed to accurately estimate the effective lateral stiffness of the combined RC frame and SF, accounting for the composite behavior. Based on the analysis results, a simple design recommendation is provided. The effectiveness of the proposed design method is then demonstrated by performing nonlinear response history analysis (NLRHA) on a four-story RC school building model.

2. Preliminary retrofit design

Before investigating the composite behavior between the SF and RC frame, the constant drift (CD) design method will be briefly introduced here. This method is discussed in detail in [41–42], and is primarily based on the displacement-based design method proposed by Priestley et al. [48]. As shown in Fig. 2a, the existing RC building is simplified from a multi-degree-of-freedom (MDOF) model into an equivalent SDOF model, where K_f is the lateral stiffness, M_{eq} is the equivalent mass, and H_{eq} is the equivalent height of the SDOF representation of the existing RC building ($SDOF_{RC}$). The equivalent damping ratio (h_{eq}) of the retrofitted system is then calculated, including the contributions of the RC frame, SF, and BRBs [49]. Although structural systems with fuller hysteretic loops will generally produce better seismic responses, a single equivalent damping ratio obtained from the peak cycle will sometimes underestimate the response. For example, a computational study [50] found that the equivalent damping obtained from the dissipated hysteretic energy under a static test at the target drift level did not correlate well to the acceleration and displacement demands from a nonlinear response history analysis. This is because the amplitude varies during earthquakes, and so an efficient solution is to use the average damping concept proposed by Newmark and Rosenbluth [51], which adopts the average equivalent damping ratio for all amplitudes up to the target displacement. This study evaluates the required stiffness of the BRB (K_d), SF (K_{SF}) and reduced h_{eq} from the $SDOF_{RC}$ model, adopting the average damping concept and secant period (T_{eq}) [52] of the structure at the target retrofit story drift. Fig. 2b depicts the SDOF model of the RC frame retrofitted with a BRB and SF.

Previous studies implementing this BRB retrofit strategy [41–43] have assumed that the RC frame, SF, and BRB act in parallel, but not compositely. In order to simplify the calculation procedure [41–43], the RC frame's lateral force–deformation relationship was assumed trilinear

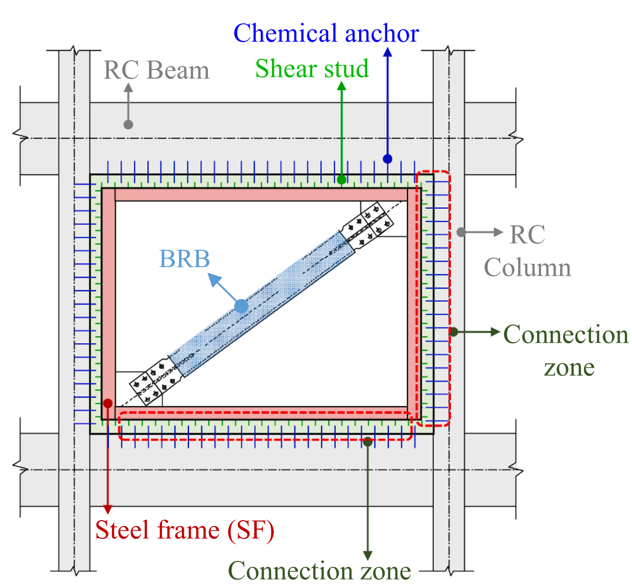

Fig. 1. Retrofit of RC frame using BRB with SF.

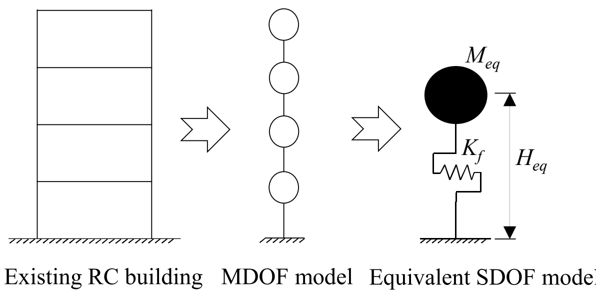

(a) Simplification of the RC building to a SDOF model

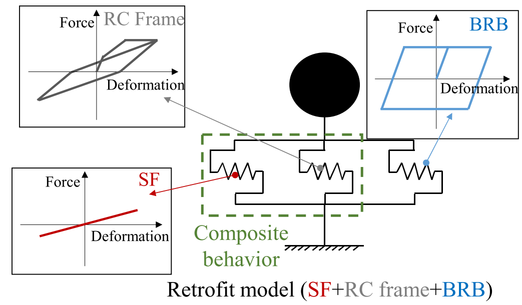

(b) Retrofitted SDOF model

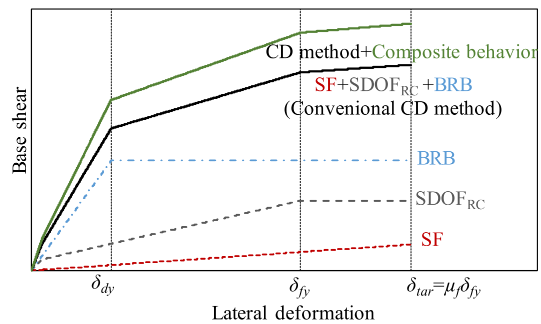

(c) Relationship between base shear and lateral deformation of the retrofitted SDOF model

Fig. 2. Simplification procedure for the analytical models.

(a) The RSB specimen

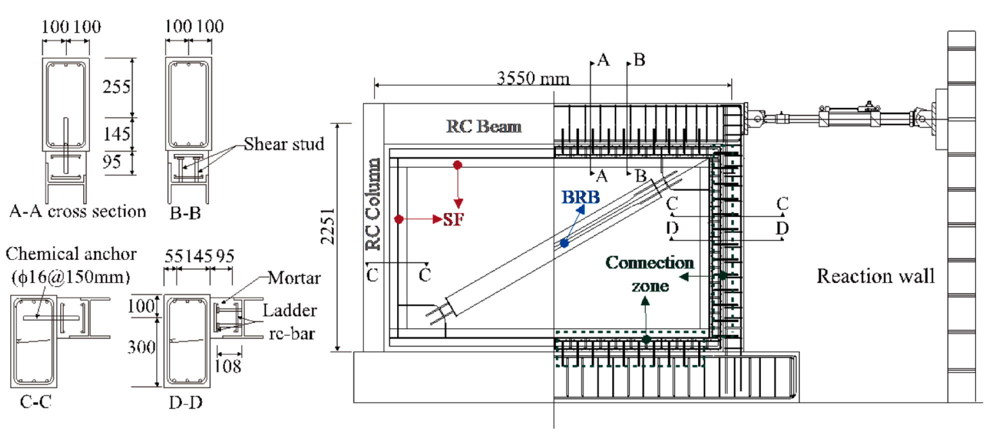

(b) Detail of the RSB specimen, connection zone cross-sections

Fig. 3. RSB specimen (Sutcu et. al.) [44]

(idealized by using the Takeda model [53]), SF was linearly elastic, and BRB was elastic-perfectly plastic, as shown in Fig. 2c. The lateral force distribution up the building height was calculated using the A_i distribution defined in the Japanese seismic design specification [54], or alternatively the equivalent static force distribution defined in ASCE-SEI7 specification [55] may be used. The numerical work presented in [56] proposed basing the force distribution on the fundamental mode shape of the retrofitted RC building. However, iteratively updating the mode shape is time-consuming. Therefore, this study uses the force distribution based on the mode shape of the retrofitted RC building, assuming that this only slightly changes due to a characteristic of the CD method where the BRB stiffness is added in proportion to RC frame stiffness at each story. The validity of this simplification is confirmed in the retrofit design example in Section 5.1.

The step-by-step retrofit design procedure of the CD method is as follows: (1) A modal pushover analysis (MPA) is conducted on the existing RC building (based on the fundamental mode shape) to obtain the roof displacement - base shear relationship. This force–displacement relationship is then simplified into a trilinear model. It is worthwhile mentioning that the pushover analysis procedure can be further simplified, as discussed in a previous study [57]. The simplified trilinear roof displacement - base shear relationship defines the $SDOF_{RC}$ model (as shown in Fig. 2c). (2) Next, the SF stiffness (K_{SF}) is assumed as 5% of BRB stiffness (K_d). The maximum displacement of the retrofitted SDOF model ($\mu_f\delta_{fy}$) is calculated for an inter-story drift ratio equal to the target story drift ratio (SDR_{tar}), which in this study is set as 1/200 rad at the design level. Note that μ_f and δ_{fy} are the displacement ductility and the lateral yield deformation of the $SDOF_{RC}$ model, as shown in Fig. 2c. (3) The corresponding reduced equivalent damping ratio (h_{eq}) and the reduced spectral displacement (δ_r) of the $SDOF_{RC}$ are then calculated. (4) At this step, the required BRB stiffness (K_d) remains as the only unknown, and is calculated by assuming that δ_r equals $\mu_f\delta_{fy}$. (5) Finally, the required BRB stiffness at the i^{th} story ($K_{d,i}$) in the MDOF model is calculated by assuming that the ratio of $K_{d,i}$ to the i^{th} story stiffness ($K_{f,i}$) equals to the ratio of K_d which was calculated in the previous step to K_f (K_d / K_f), and the i^{th} inter-story drift ratio equals SDR_{tar}. The CD method provides a fast and straightforward design procedure for practicing engineers and does not require iteration. However, the composite behavior between the RC frame and SF may significantly amplify the stiffness of the retrofitted structure, as shown in Fig. 2c. Neglecting the composite stiffness affects the required BRB stiffness ($K_{d,i}$). Therefore, this study proposes a modified CD retrofit method that includes the composite behavior, which is introduced in the following sections.

3. Numerical models simulating composite behavior

This section introduces numerical models constructed using ETABS [58], which are used to investigate the seismic performance of the retrofitted structure and composite behavior between the RC frame and SF. The numerical models are calibrated against the quasi-static cyclic loading tests conducted by Sutcu et.al. [44]. In these tests, a series of RC frame specimens with and without BRBs and SFs were cyclically loaded, representing a single perimeter bay from the 1st story of a school building that is symmetric in plan. Fig. 3a shows the test setup of the RC frame specimen retrofitted with a SF and BRB (denoted "RSB specimen"). Fig. 3b shows the details of the RSB specimen and cross-sections of the RC beams and columns. The centerline height and span of the RC frame are 2,251 mm and 3,550 mm, respectively. The compressive strength of the concrete (σ_c) is 20 MPa and the yield stress of the steel rebar is 420 MPa. Gravity load from the upper stories was included by applying a constant vertical load of 250 kN at the top of each column, which is equivalent to 15% of the column axial force capacity.

The performance of the existing RC frame (denoted "R specimen") was compared to the RC frame with a SF (denoted "RS specimen") in order to investigate the composite behavior between the RC frame and SF. Test results have shown that SF remained elastic for the RS and also RSB specimens up to 0.67% drift (1/150 rad. story drift). During the initial design, this may be confirmed by modelling the SF alone, and checking that the moment demand is less than the yield moment capacity of selected the SF section within the target story drift SDR_{tar} range. In these tests, the SF (H-175 × 175 × 7.5 × 11 mm) was fabricated using structural steel with a yield stress of 402 MPa. Out-of-plane restraints were arranged to prevent out-of-plane displacements during testing. In real buildings, existing RC slabs (i.e., rigid floor diaphragms) serve the same purpose. Although Fig. 3b shows that the SF was placed at the rear face of the RC members, which introduces eccentricity, this did not have a significant impact on the overall behavior. In [44], the test results indicated that because of the composite behavior, the combined lateral stiffness of the RC frame and SF is higher than the arithmetic total of RC frame and SF stiffness.

Fig. 3b illustrates the connection zone details between the RC frame and SF. Steel studs (13 mm diameter) were welded to the web of the SF, and chemical anchors (16 mm diameter) were embedded into the RC frame member to a depth of 145 mm. The steel studs and chemical anchors were uniformly distributed with a spacing of 150 mm, and installed in a staggered arrangement. Ladder stirrups were placed to control cracking, and the space between the SF member and RC frame was then filled with high strength mortar (80 MPa compressive strength).

The BRB in the RSB specimen is composed of a steel core made of LYP225 steel (235 MPa yield stress) and a square restrainer made of HSS 175 × 175 × 4 mm with STKR400 grade steel and infill mortar. The cross-sectional areas of the BRB in the elastic (A_e) and plastic (A_p) segments are 3,672 and 600 mm^2, respectively. This gives an axial yield force (N_y) of 141 kN. The length of the plastic segment (L_p) is 2,020 mm and each elastic (L_e) segment is 522 mm. The axial stiffness of the BRB (K_{BRB} = 54.8 kN/mm) may be calculated using Equation (1), where E = 200,000 MPa is the elastic modulus of the core.

$$K_{BRB} = 1\bigg/\left(\frac{2L_e}{A_e E} + \frac{L_p}{A_p E}\right) \tag{1}$$

These sub-assemblage frames were modelled in ETABS to investigate the effect of composite behavior between RC frame and SF, with the two-dimensional RSB model shown in Fig. 4. The test results [44] were used to validate the accuracy of the numerical models. The RC beam, columns, and the SF members are modeled by using line elements, while the composite behavior of the connection between the SF and RC frame is simplified and modelled using multi-linear plastic (MLP) links. The spacing of each MLP link was set as 150 mm to match each spacing of the chemical anchors. Fixed supports are assigned at the base. It should be noted that the out-of-plane eccentricity between the RC members and SF was not considered since it had negligible effect on the experimental seismic performance [44].

The moment–curvature relationship of the RC beams and columns was modelled obtained using the "Section Designer" tool in ETABS

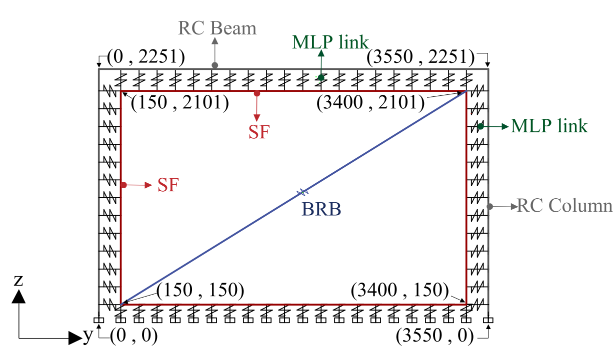

Fig. 4. Numerical model in ETABS.

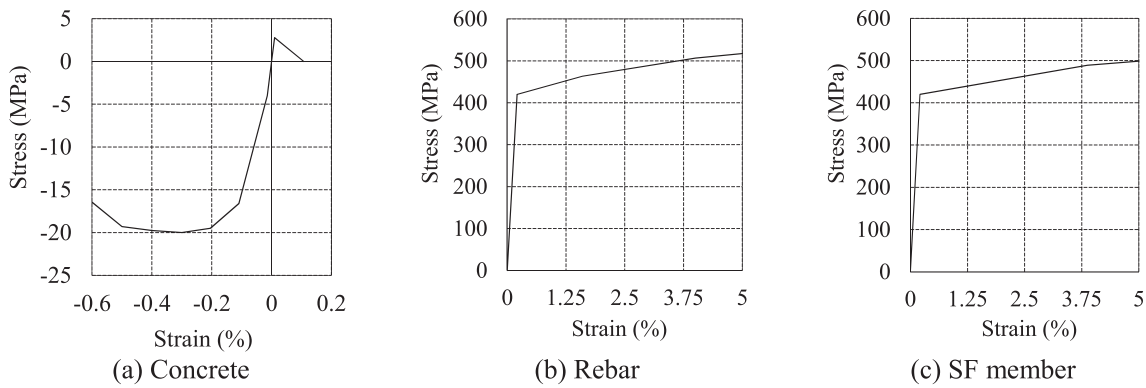

Fig. 5. Stress and strain relationships of materials.

[58]. Fig. 5a, 5b, and 5c show the stress and strain relationships for the concrete (Mander concrete model [59]), rebar, and SF, respectively. Stiffness reduction factors of 0.35 and 0.70 are assigned to the RC beam and RC columns, respectively, to represent the effective stiffness of the cracked section [60]. Each MLP link represents the composite behavior between the RC frame and SF within each spacing of the chemical anchors. Tensile "pullout" forces are resisted by the chemical anchors, while compressive forces are taken by the high strength mortar within the effective area. Based on the above assumptions, the properties of the MLP link can be defined in the following. The compressive stiffness of the mortar block (K_C = 4,400 kN/mm), as shown in Fig. 6a, is calculated as $E_m A_m / L_m$, where E_m is the elastic modulus (23,000 MPa), A_m is the contact interface area between mortar block and RC frame (150 mm × 175 mm = 26,250 mm^2), and L_m (136 mm) is the length of the high-strength mortar. As the compressive strength of the high strength mortar is higher than that the existing RC members, the compressive force capacity of the MLP link (F_C = 525 kN) is evaluated directly from the concrete strength as $\sigma_c A_m$ where σ_c is 20 MPa. Conversely, the tensile stiffness of the MLP link (K_T) is determined using an effective length equivalent to half of the embedded length (L_a). Therefore, the K_T is 555 kN/mm ($K_T = 2E_a A_a / L_a$, where E_a = 200,000 MPa is the elastic modulus of anchor material and A_a = 201 mm^2 is the cross-section area of the chemical anchor). The tensile capacity of the MLP link is represented by the tensile yield force of the chemical anchor F_T (=$\sigma_a A_a$ = 98.5 kN, where σ_a = 490 MPa is the yield stress of the chemical anchor material).

The shear stiffness of the MLP link (K_s = 1930 kN/mm), as shown in Fig. 6b, is represented by the shear stiffness of the high strength mortar within each chemical anchor spacing and is calculated by $G_m A_m / L_m$, where G_m is the shear modulus of mortar (10,000 MPa). The shear strength of the MLP link (54.5 kN) is taken as the smaller of the anchor's shear capacity determined by steel strength ($Q_{a1} = 0.7\sigma_a A_a$ = 69 kN) and bearing strength of the adjacent concrete ($Q_{a2} = 0.4(E_m \sigma_c)^{0.5} A_a$ = 54.5 kN) [61]. As Q_{a2} is smaller than Q_{a1}, the concrete near the anchor is expected to crack and lose its shear force capacity first. The axial and shear force to deformation relationships of the MLP link are shown in Fig. 6a and 6b, respectively. The MLP link element in ETABS is also used to model the BRB behavior in the RSB model. The axial stiffness and axial yield deformation of the BRB link are K_{BRB} and $\delta_{dy,\theta}$, respectively. The post-yield stiffness is assigned as 2% of the elastic stiffness, producing the axial force–deformation relationship shown in Fig. 6c. Cyclic nonlinear pushover analysis was performed on the numerical models. Fig. 7 compares the base shear to story drift response of the analyses and test results. The slight difference in the initial stiffness and strength may be attributed to the simplified material modeling and the complex nonlinear behavior of the connection zone. The effect of composite behavior is clearly reflected by these models and the accuracy is sufficient for the purposes of this investigation. Therefore, the numerical modelling method introduced in this section is used to account for the effect of composite behavior in the following sections.

4. Investigation of the composite behavior

This section introduces an evaluation approach to estimate the composite behavior between the RC frame and SF, and implements this approach in the CD method. The relationships of the stiffness amplification due to the composite behavior and the SF member section are provided. The evaluated composite behavior is then incorporated into the proposed design method in order to reduce the required BRB stiffness. A four-story RC school building located in Chiang Rai province in Thailand is used as a benchmark model to investigate the effect of composite behavior on seismic performance.

4.1. Definition of composite stiffness parameters

Two non-dimensional parameters (namely, $\gamma_{cf,i}$ and $\gamma_{cp,i}$) are defined to indicate the elastic stiffness amplification due to the composite

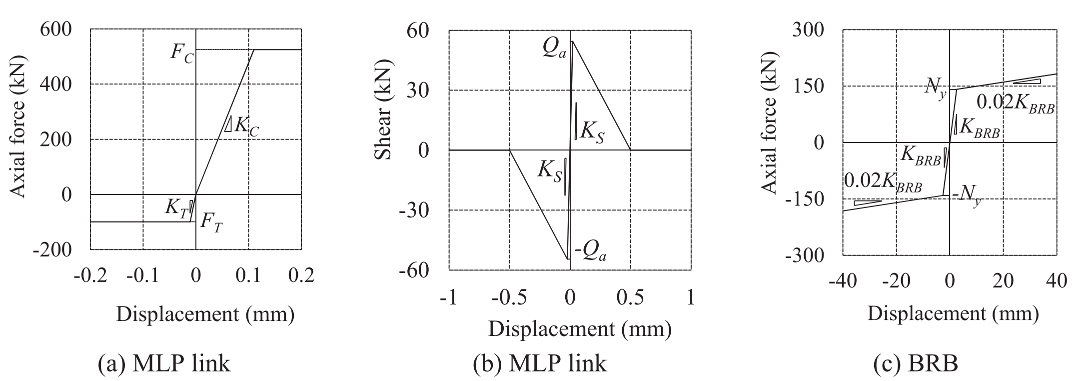

Fig. 6. Force and displacement relationships of the MLP links representing the connection zone and BRB.

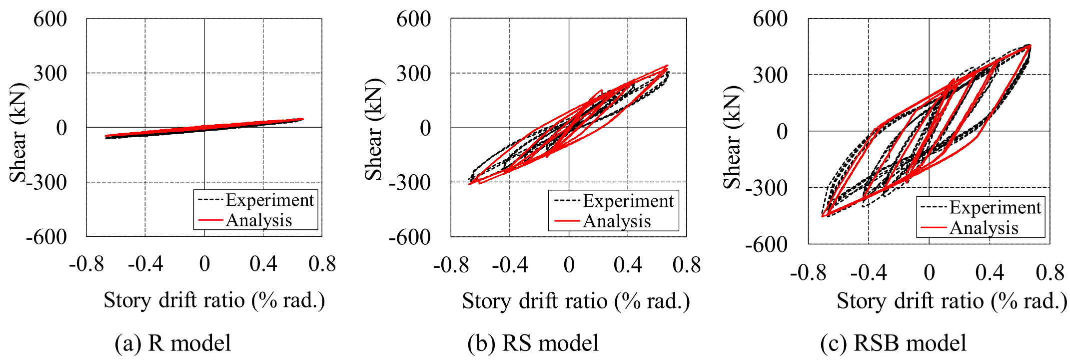

Fig. 7. Comparison of shear force and story drift ratio from experiments and analyses.

behavior. The fully composite stiffness amplification ratio ($\gamma_{cf,i}$) is defined as follows:

$$\gamma_{cf,i} = \frac{K_{Ieq,i}}{K_{RC,i} + K_{SF,i}} \geqslant 1 \tag{2}$$

where $K_{Ieq,i}$ is the i^{th} story stiffness of the retrofitted structure when RC and SF are fully composite, $K_{RC,i}$ and $K_{SF,i}$ are lateral stiffness provided by the retrofitted bay of the RC frame and SF, respectively. The value of ($K_{RC,i}$ + $K_{SF,i}$) represents the lateral stiffness provided by the RC frame and SF in the retrofitted bay acting independently (with no composite behavior). The value of $K_{Ieq,i}$ is calculated as follows:

$$K_{Ieq,i} = 1\Bigg/\left[\frac{(H_{Ieq}/2)^3}{12(EI)_{eqc,l}} + \frac{(H_{Ieq}/2)^2 l_{Ieq}}{24(EI)_{eqb,p}} + \frac{(H_{Ieq}/2)^2 l_{Ieq}}{24(EI)_{eqb,n}} + \frac{(H_{Ieq}/2)^3}{12(EI)_{eqc,r}}\right] \tag{3}$$

where $(EI)_{eqc,l}$ and $(EI)_{eqc,r}$ are the equivalent flexural rigidities of the left and right RC columns with the SF. $(EI)_{eqb,p}$ and $(EI)_{eqb,n}$ are the equivalent flexural rigidities of the RC beam and SF under positive and negative bending, as shown in Fig. 8a. It should be noted that when the structure deforms toward the right (Fig. 8a), the outer surface of the left RC column is in tension and the outer surface of the left SF column member is in compression, and vice versa for the right RC and SF columns. Thus, $(EI)_{eqc,l}$ and $(EI)_{eqc,r}$ have opposite signs. H_{Ieq} is the centerline distance between the neutral axes of the top and bottom composite beams in the relevant story. l_{Ieq} is the centerline distance between the neutral axes of the left and right composite columns. The bare RC frame stiffness $K_{RC,i}$ may be calculated as follows:

$$K_{RC,i} = 1\Bigg/\left[\frac{(H_{RC}/2)^3}{12(EI)_{cc,l}} + \frac{(H_{RC}/2)^2 l_{RC}}{24(EI)_{cb,p}} + \frac{(H_{RC}/2)^2 l_{RC}}{24(EI)_{cb,n}} + \frac{(H_{RC}/2)^3}{12(EI)_{cc,r}}\right] \tag{4}$$

where $(EI)_{cc,l}$ and $(EI)_{cc,r}$ are the flexural rigidities of the left and right RC columns, respectively. $(EI)_{cb,p}$ and $(EI)_{cb,n}$ are the flexural rigidities of the RC beam deform in positive and negative bending. The centerline story height (H_{RC}) and beam span (l_{RC}) of the RC members are shown in Fig. 8b. The steel frame stiffness $K_{SF,i}$ is calculated as follows:

$$K_{SF,i} = 1\Bigg/\left[\frac{(H_{SF}/2)^3}{12(EI)_{SFc,l}} + \frac{(H_{SF}/2)^2 l_{SF}}{12(EI)_{SFb}} + \frac{(H_{SF}/2)^3}{12(EI)_{SFc,r}}\right] \tag{5}$$

where $(EI)_{SFc,l}$ and $(EI)_{SFc,r}$ are the flexural rigidities of the left and right SF columns, while $(EI)_{SFb}$ is the flexural rigidity of the SF beam. The centerline story height (H_{SF}) and beam span (l_{SF}) of the SF members are shown in Fig. 8b. Therefore, the fully composite stiffness amplification ratio $\gamma_{cf,i}$ may be calculated analytically without a finite element model. Conversely, the partially composite stiffness amplification ratio ($\gamma_{cp,i}$) is defined as follows:

$$\gamma_{cp,i} = \frac{K_{RS,i}}{K_{RC,i} + K_{SF,i}} \geqslant 1 \tag{6}$$

where $K_{RS,i}$ is the i^{th} story stiffness obtained from the pushover analysis of the RC frame retrofitted with a SF only (RS model), including the MLP link introduced in Section 3. The value of $\gamma_{cp,i}$ indicates the stiffness amplification at the i^{th} story. The minimum possible value of $\gamma_{cp,i}$ is 1.0, which indicates that there is no or insignificant composite behavior between the RC frame and SF.

4.2. Introduction of the numerical building model

A typical four-story RC school building located in Chiang Rai province in Thailand is taken as a representative example building for this study. A three-dimensional model was constructed using ETABS. Fig. 9a and 9b show the elevation and structural plan of the RC building model, respectively. Fig. 9c shows the cross-section details of the RC beams and columns. The compressive strength of the concrete and the yield

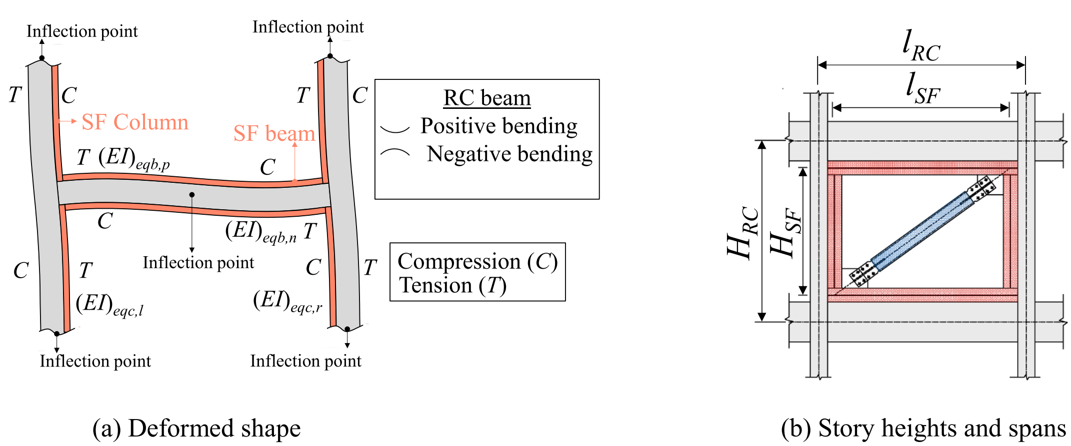

Fig. 8. Illustration of the analytical model for computing the elastic stiffness.

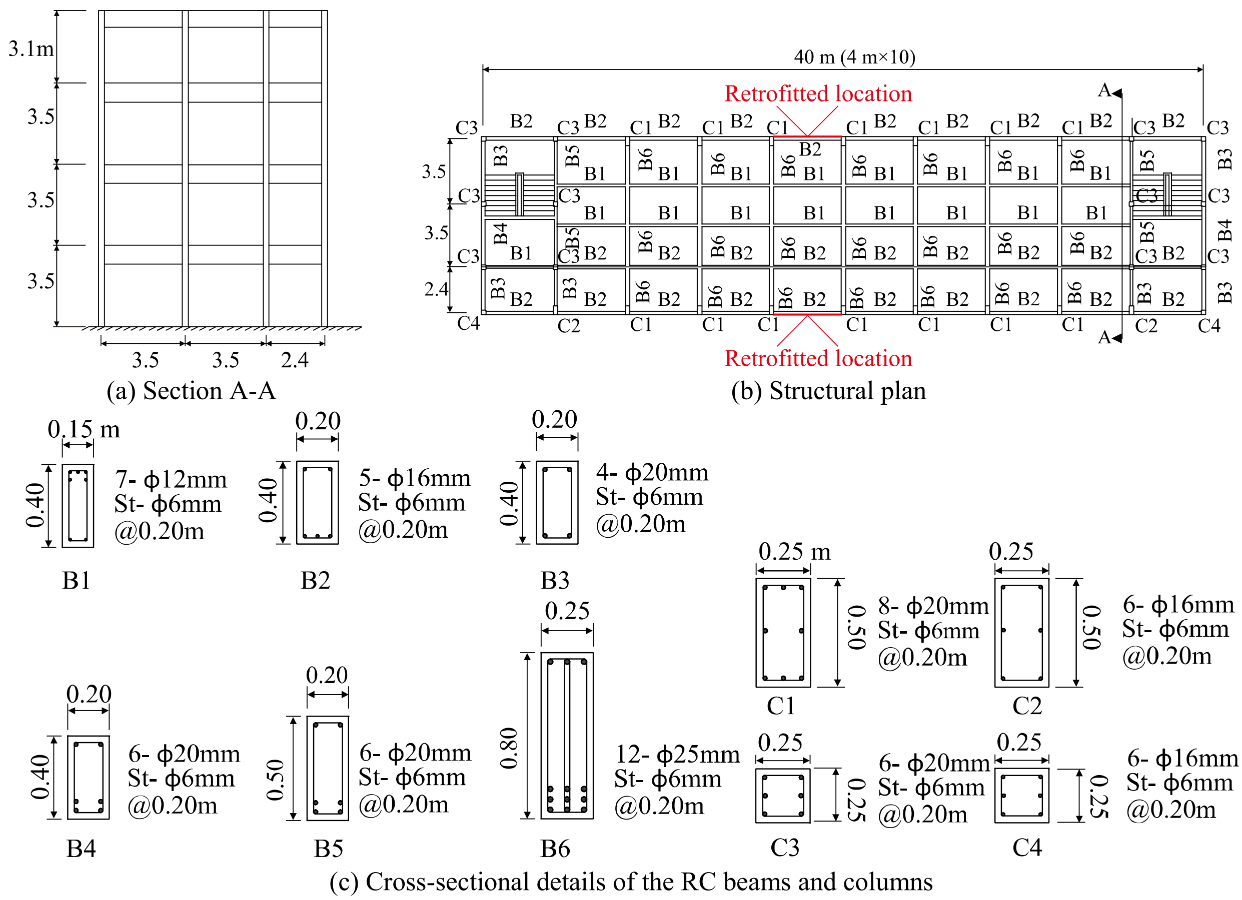

Fig. 9. Details of the four-story RC school building.

strength of the rebar are 24 and 300 MPa, respectively. The seismic mass is 184 tons for the 1st to 3rd stories and 171 tons for the 4th story. The RC concrete slab thickness is 100 mm at each story. Based on the modal analysis, the first three modes have periods of 1.249 sec (longitudinal translation), 0.871 sec (torsion), and 0.830 sec (transverse translation).

Fig. 10a and 10b depict the 5% damped design acceleration and displacement spectra for Thailand (Chiang Rai province) [62], where S_{DS} and S_{D1} are the design spectral accelerations at 0.2 sec and 1.0 sec, respectively. It is expected that the retrofit of the school building will improve the seismic performance to a level that is equivalent to immediate occupancy performance. Therefore, the maximum allowable story drift ratio of the retrofitted building is limited to 1/200 rad. (0.5% rad.).

The seismic performance of the existing RC building is evaluated using the CD method [41,42] using the SDOF$_{RC}$ model, with the H_{eq} = 10 m (73.5% of building height) and M_{eq} = 577 tons (80% of the total mass). The lateral stiffness of the SDOF$_{RC}$ model in the longitudinal ($K_{f,l}$) and transverse ($K_{f,t}$) directions are 14.6 and 33.1 kN/mm, respectively. Based on the design displacement spectrum (Fig. 10b), the spectral displacements of the SDOF$_{RC}$ model are 7.6 cm in the longitudinal ($\delta_{d,l}$) direction and 4.8 cm in the transverse ($\delta_{d,t}$) directions. As mentioned in Section 2, the CD method assumes that all MDOF interstory drifts equal the SDOF drift. The maximum story drift ratios ($SDR_{\max}$) in the longitudinal and transverse directions before retrofit are 0.76% ($=\delta_{d,l}/H_{eq}$) and 0.48% rad. ($\delta_{d,t}/H_{eq}$), respectively. As the transverse $SDR_{\max}$ (0.48% rad.) is smaller than the target 0.5% rad., retrofit is only required in the longitudinal direction in the plan, with

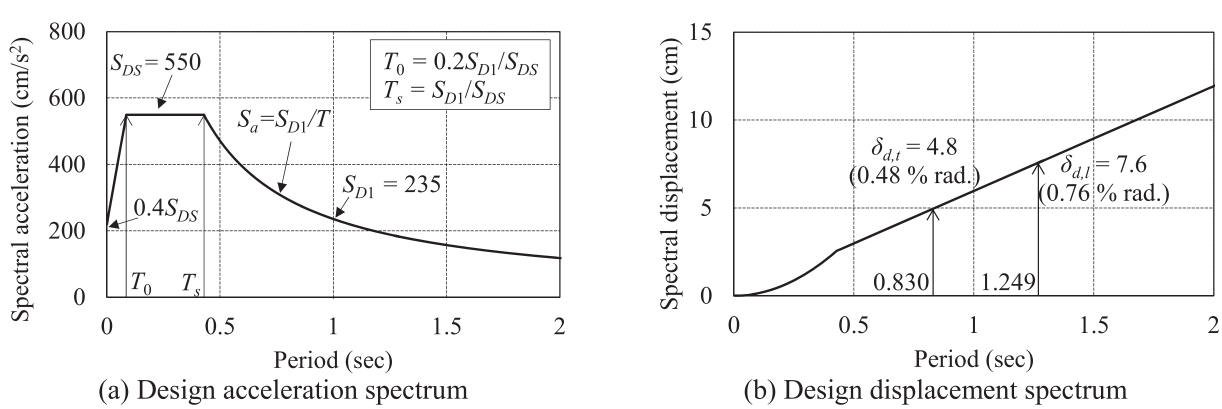

Fig. 10. Design spectra of Chiang Rai province in Thailand.

candidate retrofit locations shown in Fig. 9b. The perimeter locations are selected to minimize torsional effects and simplify installation, enabling most of the building to remain occupied and operational (i.e., no downtime) during the retrofit.

A single retrofitted bay is used to study the composite behavior between the RC frame and SF. Fig. 11 shows the two-dimensional four-story numerical RS model. It is assumed that the connection details between the RC frame and SF in the four-story retrofitted RC building, including the steel studs, chemical anchors, high strength mortar, and ladder stirrups, are consistent with the single-story test specimen presented in Section 2. Therefore, it is anticipated that the composite behavior in the four-story retrofitted RC building would be similar to the single-story RS specimen explained previously. It should be noted that the number of MLP links depends on the story height as the link spacing is fixed at 150 mm so the number of MLP links differs between the test specimen and stories of the example building.

The relationship between $\gamma_{cp,i}$ and $\gamma_{cf,i}$ with different SF section sizes are investigated. Table 1 shows the list of the SF member sections. The fully composite parameter ($\gamma_{cf,i}$) is calculated using Eqs. (2)–(5), while the partially composite parameter ($\gamma_{cp,i}$) is obtained using pushover analysis and Equations (4)–(6). The results shown in Table 1 indicate that the value of $\gamma_{cf,i}$ range from 4.7 to 7.6 and the value of $\gamma_{cp,i}$ range from 1.3 to 3.9 for the given case study.

Fig. 12 shows the linear-like relationship between $\gamma_{cf,i}$ and $\gamma_{cp,i}$ for each story according to Table 1 and also the case of no composite behavior (where, $\gamma_{cf,i} = \gamma_{cp,i} = 1$). The results indicate that the effect of composite behavior in the 1st story is greater than the upper stories. This is because the 1st story primarily experiences shear deformation due to the stiffer fixed column base, improving the composite behavior. As a result, the trend-line of the plot is proposed for two separate groups (the 1st story and upper stories). Based on the analysis results, the relationship of $\gamma_{cf,i}$ and $\gamma_{cp,i}$ is expressed as $\gamma_{cp,1} = 0.45\gamma_{cf,1} + 0.55$ for the 1st story and $\gamma_{cp,i} = 0.25\gamma_{cf,i} + 0.75$ for upper stories. Table 2 shows that the key parameters obtained from the single-story RS specimen test results fit with the proposed relation in Fig. 12.

4.3. Design recommendations

When the composite behavior is considered, the required BRB stiffness can be decreased when compared to the results obtained by the conventional CD method. Based on the previous section, the additional stiffness contribution of composite behavior can be evaluated as ($\gamma_{cp,i}$-1)($K_{RC,i} + K_{SF,i}$). Eq. (7) shows the required BRB stiffness including the composite behavior between RC frame and SF for i^{th} story ($K_{dc,i}$). When there is no composite behavior (RC frame and SF act independently), the values of $\gamma_{cp,1}$ and $\gamma_{cp,i}$ becomes 1 as the $K_{dc,i}$ will be equal to $K_{d,i}$. By substituting the proposed relationship between $\gamma_{cf,i}$ and $\gamma_{cp,i}$. Equation (7) is defined as follows:

$$\begin{aligned} K_{dc,1} &= K_{d,1} - (\gamma_{cp,1} - 1)(K_{RC,1} + K_{SF,1}) \\ &= K_{d,1} - 0.45(\gamma_{cf,1} - 1)(K_{RC,1} + K_{SF,1}) \geqslant 0 \\ K_{dc,i} &= K_{d,i} - (\gamma_{cp,i} - 1)(K_{RC,i} + K_{SF,i}) \\ &= K_{d,i} - 0.25(\gamma_{cf,i} - 1)(K_{RC,i} + K_{SF,i}) \geqslant 0 \quad \text{for } i > 1 \end{aligned} \tag{7}$$

According to the ASCE-SEI 41-17 [60] soft-story provisions, no story may have a stiffness less than 70% of the story above. This is expressed by Equation (8), where $K_{R,i}$ and $K_{R,i+1}$ are the i^{th} and the $(i+1)^{\text{th}}$ retrofitted story stiffness obtained from the pushover analysis including additional composite behavior. If the stiffness of the i^{th} story is less than 70% of the $(i+1)^{\text{th}}$ story, $K_{dc,i}$ should be replaced by $K'_{dc,i}$ to mitigate the risk of soft-story formation, producing Eq. (9).

$$\frac{K_{R,i}}{K_{R,i+1}} \geqslant 0.7 \tag{8}$$

$$\text{if } \frac{K_{R,i}}{K_{R,i+1}} < 0.7, \quad K'_{dc,i} = 0.7(K_{R,i+1} - K_{d,i+1} + K_{dc,i+1}) - K_{R,i} + K_{d,i} \tag{9}$$

The recommended retrofit design is summarized in the following steps:

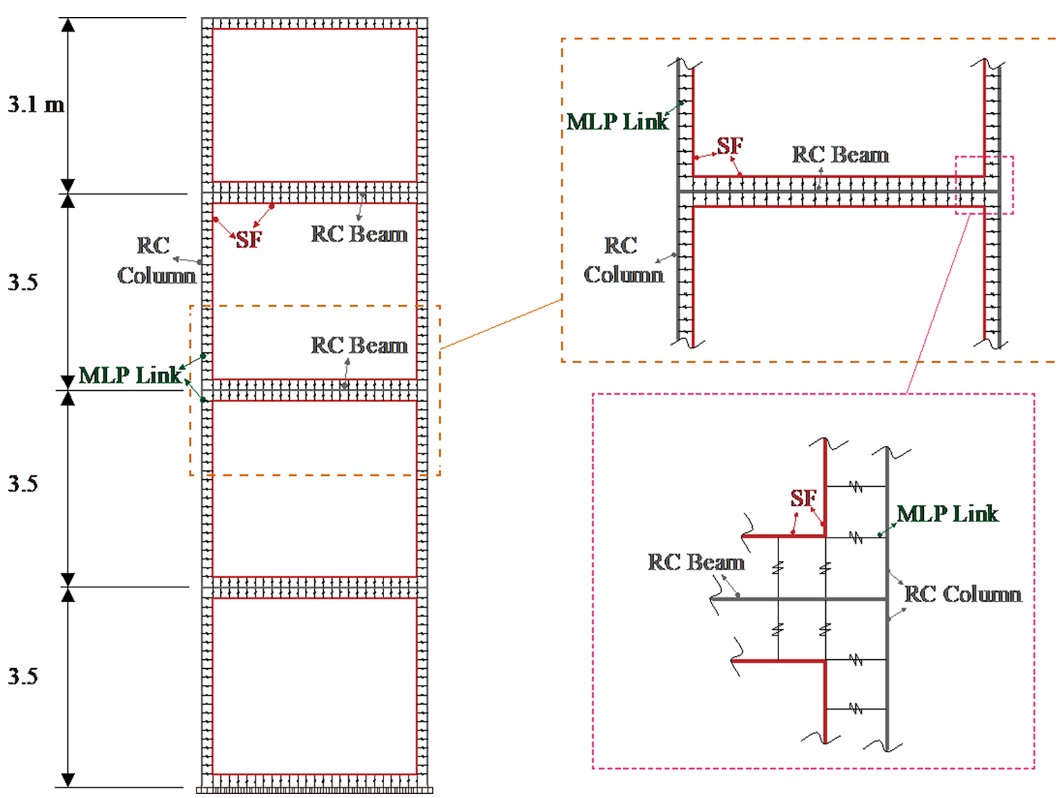

Fig. 11. The four-story numerical RS model.

Table 1
Key parameters of composite behavior with different SF member section.

SF member section (mm)	$K_{Ieq,i}$ (kN/mm)				$\gamma_{cf,i}$				$K_{RS,i}$ (kN/mm)				$\gamma_{cp,i}$			
	1st	2nd	3rd	4th	1st	2nd	3rd	4th	1st	2nd	3rd	4th	1st	2nd	3rd	4th
100 × 100 × 6 × 8	17.5	17.5	17.5	20.8	5.1	5.1	5.1	4.7	9.3	6.7	6.3	7.1	2.7	2.0	1.9	1.6
125 × 125 × 6.5 × 9	22.3	22.3	22.3	25.5	6.1	6.1	6.1	5.4	11.6	8.4	7.9	8.4	3.2	2.3	2.2	1.8
150 × 150 × 7 × 10	27.9	27.9	27.9	30.9	6.9	6.9	6.9	5.8	14.4	10.5	9.7	10.0	3.5	2.6	2.4	1.9
175 × 175 × 7.5 × 11	34.5	34.5	34.5	37.6	7.4	7.4	7.4	6.1	18.0	13.1	12.2	12.0	3.9	2.8	2.6	1.9
200 × 200 × 8 × 12	42.4	42.4	42.4	45.6	7.6	7.6	7.6	6.2	21.8	15.7	14.2	13.9	3.9	2.8	2.5	1.9
200 × 250 × 9 × 14	60.8	60.8	60.8	60.5	7.1	7.1	7.1	5.2	31.7	22.9	20.5	18.5	3.7	2.7	2.4	1.6
200 × 300 × 9 × 15	80.7	80.7	80.7	84.0	6.2	6.2	6.2	4.7	44.1	30.9	27.6	23.6	3.4	2.4	2.1	1.3

1. Perform the pushover analysis to obtain $K_{f,i}$.
2. Calculate $K_{d,i}$ based on $K_{f,i}$ from the preliminary design.
3. Select the SF section and calculate $K_{SF,i}$ from Equation (5) so that $K_{SF,i}$ is either equal or slightly greater than 5% of $K_{d,i}$.
4. Obtain $K_{RC,i}$ for each retrofitted frame using Equation (4) or by performing pushover analysis.
5. Calculate the $K_{dc,i}$ from Equation (7) that satisfies the required stiffness, considering the composite behavior between the RC frame and SF.
6. Design the BRBs with lateral stiffness equal to or greater than $K_{dc,i}$. The lateral yielding deformation (δ_{dy}) may be determined from the maximum allowable elastic story drift.
7. Obtain the retrofitted story stiffness ($K_{R,i}$) by performing pushover analysis of the retrofitted building. If a soft-story occurs in the i^{th} story, $K_{dc,i}$ should be replaced by $K'_{dc,i}$ from Equation (9).

5. Retrofit examples and analysis results

Table 3 shows the design results of the retrofitted four-story RC school building. $K_{f,i}$ is obtained by performing pushover analysis for the three-dimensional model of the existing building (3D-R model). $K_{d,i}$ is calculated following the procedure mentioned in Section 2. Based on this preliminary design, the lateral stiffness of the 4th story BRBs ($K_{d,4}$) required to achieve the design requirement of SDR_{tar} of 0.5% rad. is less than 0, and so there is no need to install BRBs in the 4th story. This will be confirmed using NLRHA in the following sections. The selected SF section sizes for all models are 175 × 175 × 7.5 × 11 mm for the 1st and 3rd stories, and 200 × 200 × 8 × 12 mm for the 2nd story, which are selected based on $K_{d,i}$. $K_{SF,i}$ is calculated based on Equation (5). The i^{th} story stiffness of the retrofitted RC frame ($K_{RC,i}$) is obtained from Equation (4) and compared to the pushover results in Table 3. The axial stiffness of the BRBs in the i^{th} story ($K_{BRB,i}$) may be determined from $K_{dc,i}$. As shown in Table 3, the required BRB stiffness considering composite behavior ($K_{dc,i}$) is smaller than those when composite behavior is neglected ($K_{d,i}$). The strength of the BRB may be determined from the BRB axial yield deformation and $K_{BRB,i}$. The BRB lateral yield deformation (δ_{dy}) is calculated as follows:

$$\delta_{dy} = \left[\frac{(A_e/A_p)(L_{BRB}/L_p) - (L_{BRB}/L_p) + 1}{(A_e/A_p)}\right]\frac{L_{BRB}\varepsilon_y}{\cos\theta_{BRB}} \tag{10}$$

where L_{BRB} is the BRB work-point to work-point length, ε_y (0.12%, SN400B steel grade) is the yield strain of the BRB steel core material, and θ_{BRB} is the inclination angle of the BRB. In this retrofit design example, the ratios of A_e/A_p and L_p/L_{BRB} are 4 and 0.5, which are representative of conventional BRB designs [42]. Furthermore, by maintaining constant A_e/A_p and L_p/L_{BRB} ratios, the yield deformation δ_{dy} remains unchanged when replacing $K_{d,i}$ with $K_{dc,i}$.

Fig. 13 and Table 4 show the BRB designs where each BRB is named by the numerical model type and story number. For example, the BRB sizes and yield capacities where composite behavior is neglected are denoted RSB1, RSB2, and RSB3 for the 1st, 2nd, and 3rd stories. Similarly, designs considering composite behavior is denoted RSCB1, RSCB2 and RSCB3. All the BRB steel cores are made of SN400B grade steel with a yield strength of 235 MPa. The restrainers are made by using an HSS square tube made of STKR400 steel and infill mortar with a compressive strength of 55 MPa. It should be noted that the proposed design method including composite behavior provides a realistic combined lateral stiffness of the RC frame and SF. Therefore, the required BRB stiffness is more precisely estimated, and the design economy is improved. The required weights of BRBs (W_{BRB}) are calculated by the total steel weight of the elastic, plastic, and restrainer segments. If the W_{BRB} in the 3D-RSCB model is compared to the W_{BRB} in 3D-RSB model, the W_{BRB} can be reduced by 28%, 16% and 11% in the 1st, 2nd and 3rd stories, respectively. This is a significant outcome of the proposed method in terms of economy.

To confirm the seismic performance of the retrofitted building, three numerical models were developed, with the existing building model (3D-R) used as a benchmark. The performance of the retrofitted models designed using the conventional CD method neglecting composite

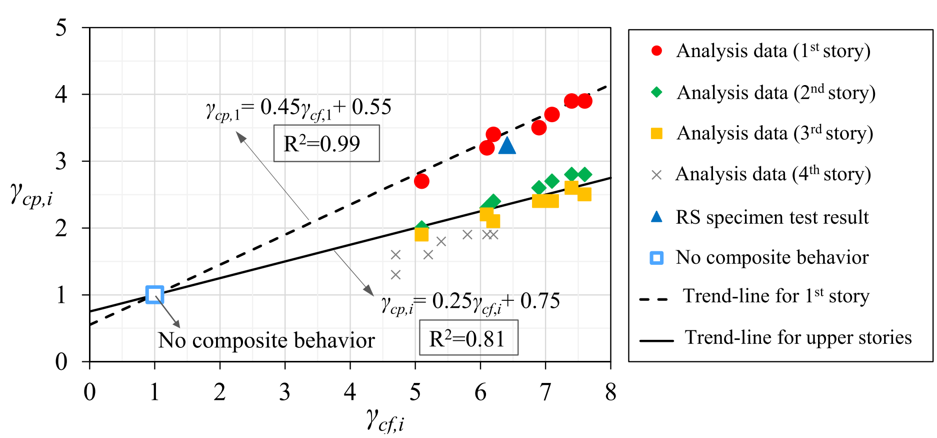

Fig. 12. Relationship between $\gamma_{cf,i}$ and $\gamma_{cp,i}$.

Table 2
Key parameters obtained from the experiments on the single-story RS specimen.

K_{RC} (kN/mm) (Equation (4))	K_{SF} (kN/mm) (Equation (5))	K_{Ieq} (kN/mm) (Equation (3))	γ_{cf} (Equation (2))	K_{RS}* (kN/mm) (Pushover analysis)	γ_{cp} (Equation (6))
8.46	5.51	89.52	6.41	45.24	3.24

K_{RS}* is obtained from the experiment.

Table 3
Design results.

Story	Before retrofit	CD method	Proposed method				
	$K_{f,i}$ (kN/mm)	$K_{d,i}$ (kN/mm)	$K_{RC,i}$ (kN/mm)		$\delta_{dy,i}$ (mm)	$K_{SF,i}$ (kN/mm)	$K_{dc,i}$ (kN/mm)
	Pushover analysis	[41,42]	(Equation (4))	Pushover analysis	(Equation (10))	(Equation (5))	(Equation (7))
4th	39.6	–	4.1	3.7	–	–	–
3rd	32.2	34.8	3.2	3.0	3.5	2.0	26.5
2nd	32.1	65.4	3.2	3.1	3.5	3.8	53.9
1st	45.3	43.7	3.2	4.3	3.5	2.0	28.7

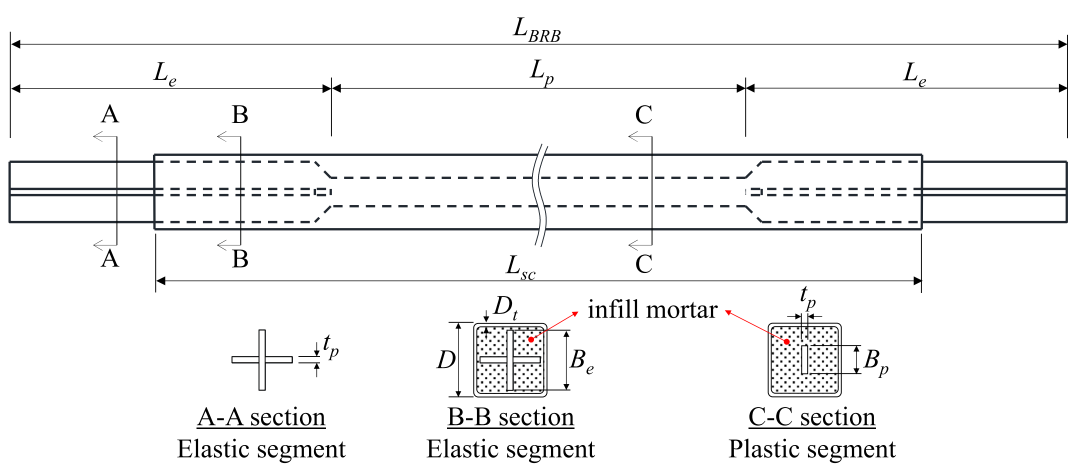

Fig. 13. Profile of the BRB member.

Table 4
Design details of the BRB members.

BRB member	Axial force	Plastic segment				Elastic segment			Restrainer segment			Weight
	N_y (kN)	t_p (mm)	B_p (mm)	A_p (mm^2)	L_p (mm)	B_e (mm)	A_e (mm^2)	L_e (mm)	L_{sc} (mm)	D (mm)	D_t (mm)	W_{BRB} (kgf)
RSB1	133.95	10	57	570	2534	119	2280	1267	3801	150	3.2	113
RSB2	199.75	10	85	850	2517	175	3400	1258	3775	200	4.5	188
RSB3	108.1	10	46	460	2534	97	1840	1267	3801	120	6	127
RSCB1	82.25	10	35	350	2534	75	1400	1267	3801	125	3.2	81
RSCB2	159.8	10	68	680	2517	141	2720	1258	3775	175	4.5	158
RSCB3	75.2	10	32	320	2534	69	1280	1267	3801	120	6	113

behavior (3D-RSB) and including composite behavior (3D-RSCB) are then compared to the unretrofitted benchmark model. The mechanical properties of the MLP links for the 3D-RSB and 3D-RSCB models are identical to the RS model introduced in Section 4.2. Fig. 14a and 14b show the analysis model and a perimeter elevation.

5.1. Modal analysis

Fig. 15a shows the periods of the first three longitudinal translational modes. The modal analysis indicates that the fundamental periods decrease from 1.249 sec (3D-R) to 0.78 sec for the 3D-RSB model and to 0.82 sec for the 3D-RSCB model. The modal analysis suggests that there are only minor differences in the fundamental mode shapes (Fig. 15b) between the three models. This supports the initial assumption that the change in the mode shape after retrofit is insignificant.

5.2. Modal pushover analysis (MPA)

Modal pushover analysis (MPA) is performed for each model using the respective fundamental mode shapes to obtain the elastic story stiffness and force–deformation relationships. The elastic story stiffness is shown in Table 5 for each model, and the story shear forces and deformation relationships are shown in Fig. 16a, 16b and 16c for the

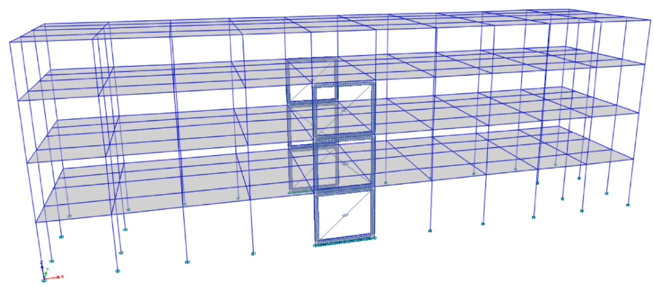

(a) 3-D view of the analysis model

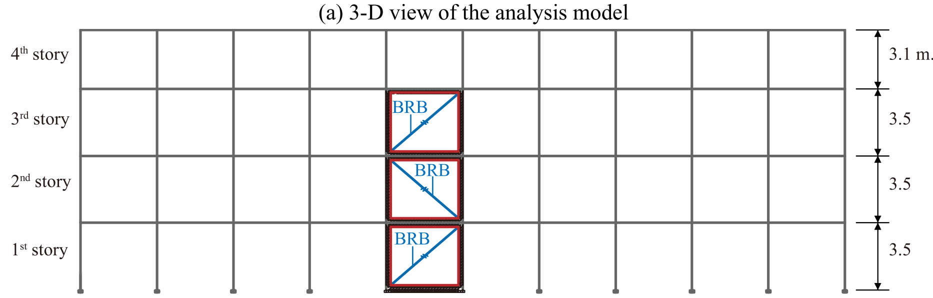

(b) Structural elevation with the components of the retrofitted bay

Fig. 14. The retrofitted RC building model.

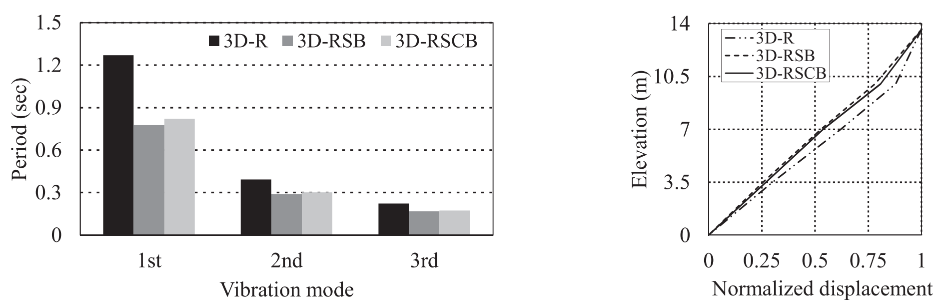

(a) Vibration periods for translation mode (b) Translation mode shape

Fig. 15. Modal analysis results for longitudinal direction (retrofit direction).

Table 5
Elastic story stiffness (kN/mm).

Story (i)	3D-R ($K_{f,i}$)	3D-RSB	3D-RSCB ($K_{R,i}$)	$K_{R,i}/K_{R,i+1}$
4th	39.6	51.8	50.7	1.49
3rd	32.2	81.7	75.5	1.32
2nd	32.1	109.3	99.7	1.13
1st	45.3	126.1	112.4	–

3D-R, 3D-RSB and 3D-RSCB models, respectively. The results show that the elastic story stiffness of the retrofit models (3D-RSB and 3D-RSCB models) has increased. In addition, the story stiffness of all adjacent stories satisfy the soft-story requirements (Equation (8)).

5.3. Nonlinear response history analysis (NLRHA)

Nonlinear response history analysis (NLRHA) is also performed for the 3D-R, 3D-RSB, and 3D-RSCB models using a suite of eleven ground motions to investigate the seismic response and validate the proposed retrofit design method. The seismic performance of each model is evaluated using the mean and mean plus one standard deviation (SD) of the analysis results for different ground motion records.

5.3.1. Ground motions for NLRHA

The suite of eleven records is selected from the PEER NGA West 2 ground motion database [63]. Only the first horizontal component is used as only the response in the retrofitted longitudinal direction is of interest to the section and the torsional response is low. The selected ground motions are shown in Table 6 and the scaled spectra are shown in Fig. 17. Amplitude scaling is conducted over a target period range of 0.2 T_1 and 1.5 T_1, which follows the ASCE 7–16 [55] requirements, where T_1 (1.249 sec) is the fundamental period of the 3D-R model, resulting in a target period range of 0.250 to 1.874 sec. The records are limited to strike-slip events with magnitudes of 6 ≤ M_w ≤ 7.5 within 20 km, which is consistent with the dominant seismic hazard of the Chiang Rai province in Thailand, where the target building is located. Records were further limited to soil class D (180 ≤ $V_{s,30}$ ≤ 360 m/s), which matches the local site conditions. The record scale factors vary from 0.68 to 1.89, and the average spectrum is at least 90% of the design spectrum over the target period range.

5.3.2. Maximum inter-story drift ratio

The maximum mean and mean plus one standard deviation inter-story drift ratio (SDR_{max}), for each ground motion, for the 3D-R, 3D-RSB, and 3D-RSCB models are shown in Fig. 18a, 18b, and 18c, respectively. Fig. 18a shows the SDR_{max} of the building without retrofit. The SDR_{max} in the 1st to 3rd stories exceeds the SDR_{tar} (0.5% rad.) for all ground motions. This confirms the previous conclusion from Table 3 that no BRBs are required in the 4th story. Fig. 18b shows the SDR_{max} of the 3D-RSB model, which was designed neglecting the composite

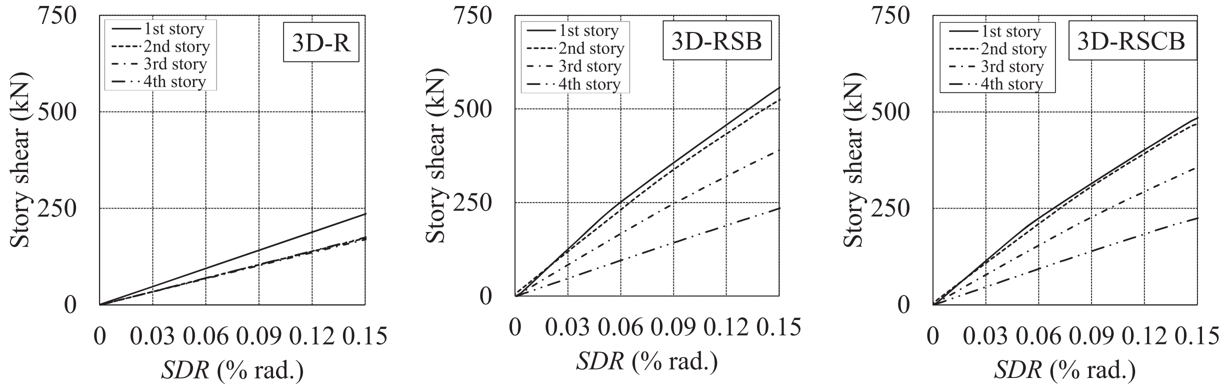

(a) 3D-R model (b) 3D-RSB model (c) 3D-RSCB model

Fig. 16. Relationship between story shear and inter-story drift ratio.

Table 6
Ground motions used for NLRHA.

Ground motion (GM) ID	Earthquake Name	Year	Station Name	Magnitude	Scaling factor
1	Imperial Valley-06	1979	Delta	6.5	0.85
2	Imperial Valley-06	1979	El Centro Array #13	6.5	1.89
3	Superstition Hills-02	1987	Plaster City	6.5	1.69
4	Superstition Hills-02	1987	Westmorland Fire Sta	6.5	1.11
5	Landers	1992	Desert Hot Springs	7.3	1.34
6	Landers	1992	North Palm Springs	7.3	1.57
7	Kobe_Japan	1995	Sakai	6.9	1.32
8	El Mayor-Cucapah_ Mexico	2010	Bonds Corner	7.2	1.16
9	El Mayor-Cucapah_ Mexico	2010	Calexico Fire Station	7.2	0.91
10	El Mayor-Cucapah_ Mexico	2010	Holtville Post Office	7.2	1.20
11	Darfield_ New Zealand	2010	DFHS	7.0	0.68

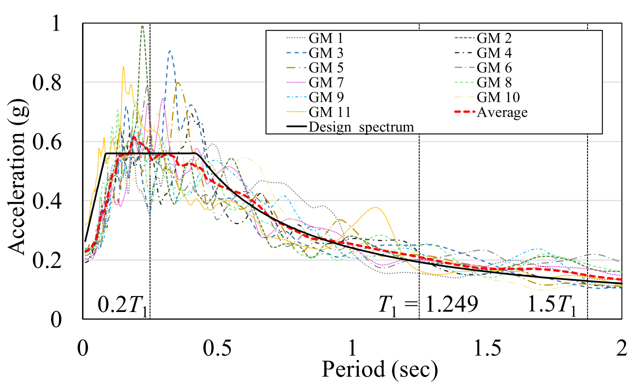

Fig. 17. The 5% damped response spectra of the scaled ground motions and the design acceleration spectrum.

behavior (conventional CD method). Fig. 18c shows the $SDR_{\max}$ of the 3D-RSCB model, which was designed using the proposed method including the composite behavior (modified CD method). The analysis results indicate that the BRB stiffness designed using both methods efficiently limit the drift responses to less than the target of 0.5% rad. where the average drift result of the proposed design method is slightly closer to the target limit. On the other hand, both models implement the same SF sections and the 3D-RSCB model achieves the SDR_{tar} limit using less BRB stiffness compared to the 3D-RSB model. This may be attributed to the fact that the SF member sizes were not changed in conjunction with the reduced BRB stiffness in the proposed design method.

5.3.3. Residual story drift ratio

The residual story drift ratio (SDR_{re}) is closely related to post-earthquake damage assessment [64]. The permissible residual deformation levels consider building functionality, construction tolerances, and safety, and is taken as 0.005 rad. (0.5% rad.) following [65].

Schools are essential public places, and some countries use school buildings as post-disaster shelters. Therefore, these buildings are typically designed to a higher importance factor and ideally should be capable of returning to full operational capacity immediately after an earthquake event. In this study, the residual drift was obtained after 60 sec of free vibration at the end of each ground motion data. The mean and mean plus one standard deviation SDR_{re} of the 3D-R, 3D-RSB, and 3D-RSCB models are shown in Fig. 19a, 19b, and 19c, respectively. SDR_{re} is efficiently reduced for the RC building retrofitted with BRBs (3D-RSB and 3D-RSCB models) when compared to the existing RC building (3D-R model). The analysis results indicate that the SDR_{re} are limited to less than 0.1% for the 3D-RSB and 3D-RSCB models, which are much smaller than the target value of 0.005 rad. This result shows that proposed retrofit has the effect of reducing both structural and nonstructural damage in the 3D-RSB and 3D-RSCB models, and increases the likelihood of the retrofitted buildings returning to operational capacity immediately after the earthquake event.

5.3.4. Energy dissipation performance of BRBs

The ductility demand and energy dissipation performance are key considerations for BRBs. These are indicated by the BRB displacement ductility (μ_d), which is calculated as the ratio of the maximum axial work-point deformation to the yield deformation, and the energy dissipation ratio ($R_E = E_d / E_I$), where E_d is the hysteretic energy dissipated by the BRBs and E_I is the total input energy. Yielding and plastic energy dissipation occur for μ_d greater than 1. Fig. 20a and 20b show the NLRHA ductility demands for all ground motions, which ranged from $\mu_d = 2.01$ to 3.22 for the 3D-RSB model and $\mu_d = 2.13$ to 3.27 for the 3D-RSCB model. Fig. 21 shows the energy dissipation ratio R_E

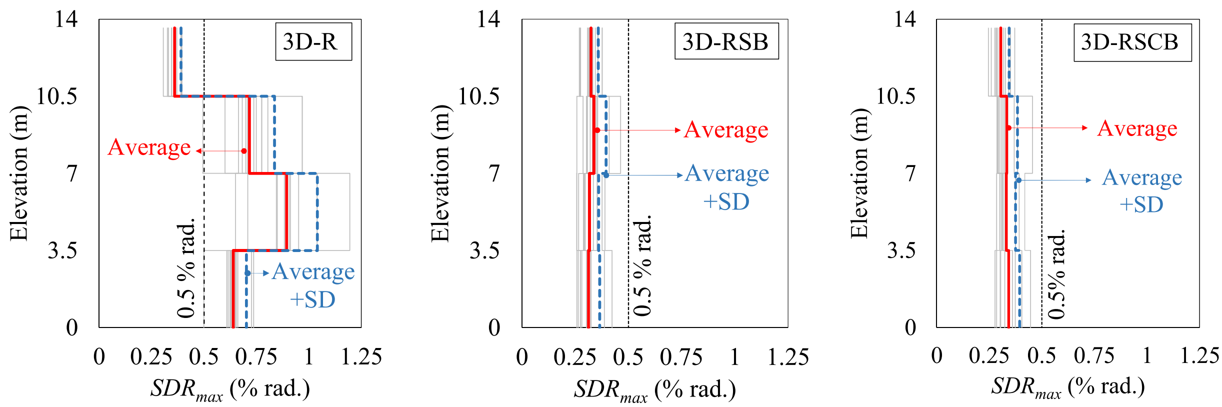

(a) 3D-R model (b) 3D-RSB model (c) 3D-RSCB model

Fig. 18. Maximum inter-story drift ratio.

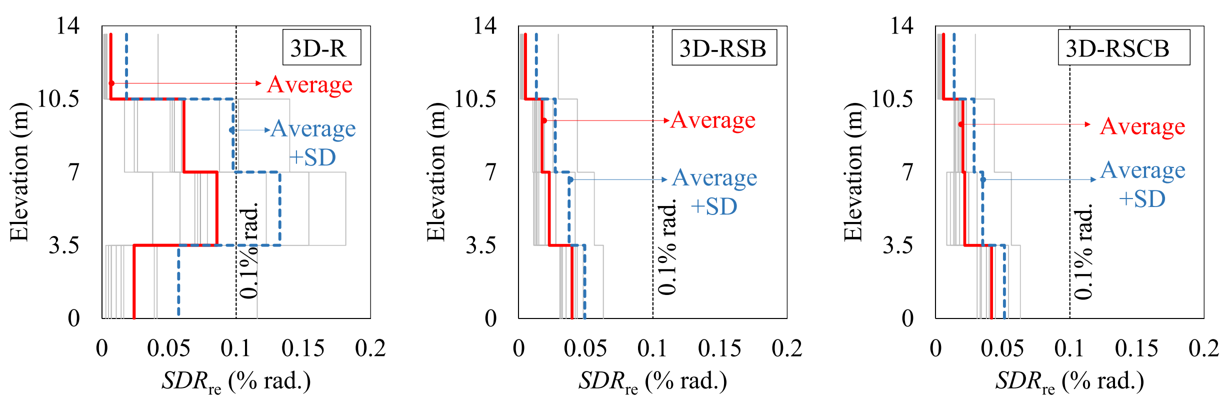

(a) 3D-R model (b) 3D-RSB model (c) 3D-RSCB model

Fig. 19. Residual story drift ratio.

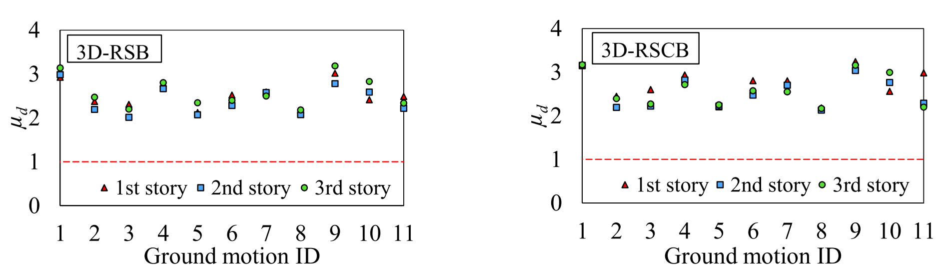

(a) 3D-RSB model (b) 3D-RSCB model

Fig. 20. Ductility of BRB.

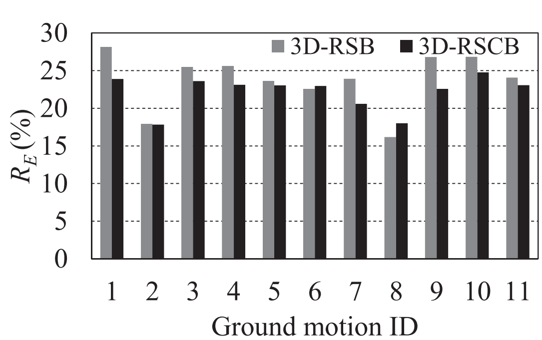

Fig. 21. Ratio of energy dissipated by the BRBs to the total input energy.

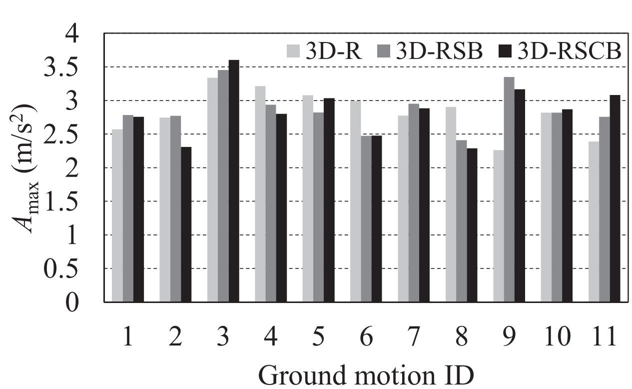

Fig. 22. Maximum roof acceleration.

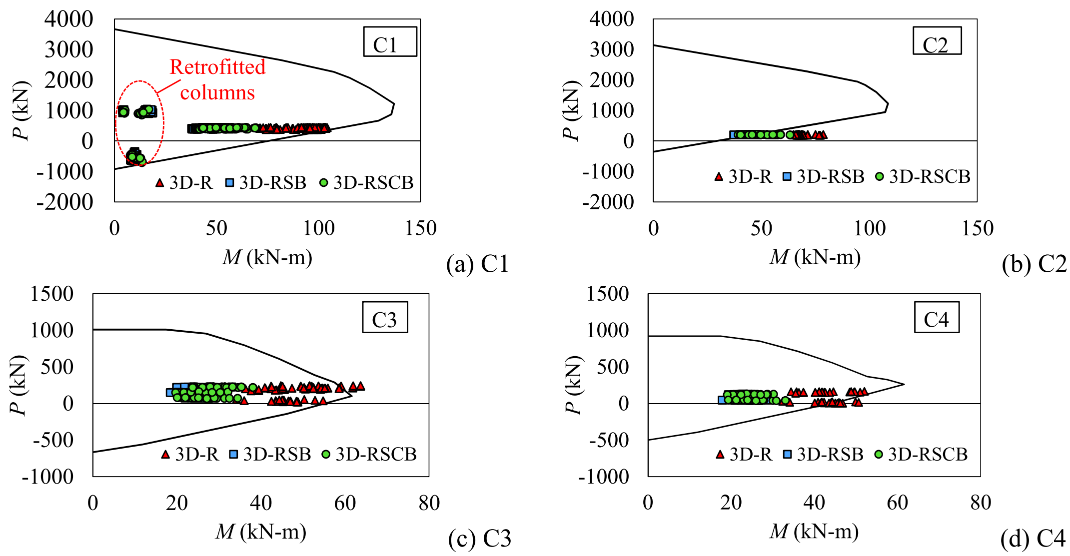

Fig. 23. P-M interaction diagrams and the maximum bending and axial force demands for the columns.

obtain from the NLRHA of all ground motions for the 3D-RSB and 3D-RSCB models. The six BRBs (1st story to the 3rd story, two frame elevations) dissipated around 20% of the total input energy. As shown in Fig. 21, the R_E ratios of 3D-RSCB models are generally smaller than the 3D-RSB models. This occurs because the BRBs in the 3D-RSCB model are less stiff than those in the 3D-RSB model given equal BRB yield drifts and maximum drifts.

5.3.5. Maximum roof acceleration

The additional stiffness introduced by the BRBs may increase the maximum roof acceleration ($A_{\max}$) in the retrofitted buildings, following the acceleration design spectrum. However, a reduction in $A_{\max}$ is also expected due to the energy dissipated by the BRBs, and so net effect should be confirmed after retrofitting a building with BRBs. Fig. 22 shows $A_{\max}$ for the 3D-R, 3D-RSB, and 3D-RSCB models from the NLRHA. The variability in the response may be attributed to the different ground motion characteristics. Based on the analysis results, only minor differences were observed in the maximum roof acceleration before and after retrofitting the building.

5.3.6. Seismic demand on columns

The existing strength of the RC columns may be a concern when a retrofit increases the lateral force demand or redirects axial load into the existing columns. The combined axial and bending moment interactions (P-M interaction) of the RC columns are used to confirm the columns' capacities following the retrofit. Fig. 23 superimposes the peak bending moment (M) and simultaneous axial force (P) demands experienced by the 14 × C1, 2 × C2, 12 × C3, and 2 × C4 columns (Fig. 9b) with their P-M capacity diagrams, considering compressive forces as positive. The analysis results show that the bending moment demands are significantly reduced in the retrofitted models (3D-RSB and 3D-RSCB models) due to the smaller $SDR_{\max}$. It should be noted that although the C2 bending moment demands are reduced following retrofit, these remain slightly larger than their capacities even after retrofit (Fig. 23b), and so strengthening is required. The greater reduction in P-M demand is achieved for the C1 columns adjacent to the retrofitted bays, as the bending moment demand is reduced due to the smaller drift, while the increased axial force due to composite behavior remains a small fraction of the axial force capacity. As shown in Fig. 23a, tensile forces are observed in the columns adjacent to the retrofitted bay. However, these columns should exhibit stable lateral stiffness and strength when acting together with the SF columns. Based on the NLRHA results, it may be concluded that the effects of the additional seismic demands on the original RC structure implementing the proposed retrofit may be mitigated.

5.4. Summary

According to the analysis results, the seismic performance of the RC building was efficiently improved using a retrofit scheme consisting of BRBs and steel frames (SF). The relative seismic performance of the example retrofitted buildings indicate that comparable performance may be achieved with smaller BRBs if composite behavior between the SF and RC frame is considered. This suggests that there is a significant advantage in including composite behavior when designing BRB and SF retrofits of RC buildings. In this case study, including the composite behavior reduced the required BRB steel tonnage W_{BRB} by around 20%.

6. Conclusions

This study investigated the influence of composite behavior between an existing RC frame and new steel frame (SF) on the seismic performance of the BRB retrofitting scheme. Based on the analysis results of detailed numerical models, an improved design method was proposed, along with recommendations to estimate the composite behavior. The following conclusions may be drawn:

(1) When retrofitting existing RC buildings using a SF, the composite behavior activated by the connection between the RC frame and SF may significantly increase the combined lateral stiffness.
(2) The composite behavior between the RC frame and SF was modeled using MLP links in ETABS, and equations proposed to quantify the link properties. The obtained analysis results are in good agreement with the experimental results of single-story specimens under cyclic loading.
(3) An approximate equation for estimating the stiffness contribution of the composite behavior is proposed according to the relationship between fully and partially composite stiffness amplification ratios. This relationship is proposed based on a series of pushover analysis results and a single-story specimen test result. It is found that 1st story generally exhibits greater composite behavior than the upper stories due to the fixed columns providing a stronger boundary condition.
(4) The reduction of BRB stiffness is evaluated by the additional stiffness contribution due to the composite behavior. The BRB design can be more economic when composite behavior is considered

according to the RC school building case study. Based on the example building, the BRBs steel tonnage can be reduced by 20% compared to a retrofit design that does not consider composite behavior.

7. Author statement

Each author's statement for the above manuscript is as follows.

Panumas Saingam has carried out analyses and studies, and created the main document and responsible to the whole research results.

Fatih Sutcu has conducted physical test referred in this manuscript, and advised Panumas Saingam on the whole research works, suggesting the composition of the research and manuscripts.

Yuki Terazawa has supported Panumas Saingam in constructing analysis models.

Kazuhiro Fujishita has been involved in the physical test referred in this manuscript, and advised analyzing the test data and constructing the study models.

Pao-Chun Lin has also advised on analysis methods, and whole manuscripts.

Oguz C. Celik was the supervisor of this research project in Turkey side, including the physical cyclic test used for this research.

Toru Takeuchi was the supervisor of this research project in Japan side, managing the whole research project and suggesting the manuscript constitution.

Declaration of Competing Interest

The authors declare that they have no known competing financial interests or personal relationships that could have appeared to influence the work reported in this paper.

References

[1] Mitchell D, DeVall RH, Saatcioglu M, Simpson R, Tinawi R, Tremblay R. Damage to concrete structures due to the 1994 Northridge earthquake. Can J Civ Eng 1995;22:361–77.

[2] Mitchell D, DeVall RH, Kobayashi K, Tinawi R, Tso WK. Damage to concrete structures due to the January 17, 1995, Hyogo-ken Nanbu (Kobe) earthquake. Can J Civ Eng 1996;23:757–70.

[3] Tsai K.C, Hwang S.J. Seismic Retrofit Program for Taiwan School Buildings After FTER 1999 Chi-Chi Earthquake. 14th World Conference on Earthquake Engineering 2008.

[4] Lukkunaprasit P, Ruangrassamee A, Boonyatee T, Chintanapakdee C, Jankaew K, Thanasisathit N, et al. Performance of Structures in the Mw 6 1 Mae Lao Earthquake in Thailand on May 5 2014 and Implications for Future Construction. J Earthquake Eng 2015;20:219–42.

[5] Celik OC. Holistic Seismic Behavior and Design of Buildings. FACADE Conference 2017:161–73.

[6] Masi A, Chiauzzi L, Santarsiero G, Manfredi V, Biondi S, Spacone E, et al. Central Italy earthquake the Amatrice case study. Bull Earthq Eng 2016;2019(17):5631–54.

[7] Applied Technology Council for the Federal Emergency Management Agency. Next-Generation Methodology for Seismic Performance Assessment of Buildings, FEMA 2012. Report No. FEMA P-58.

[8] Cosenza E, Vecchio CV, Ludovico MD, Dolce M, Moroni C, Prota A, et al. The Italian guidelines for seismic risk classification of constructions: technical principles and validation. Bull Earthq Eng 2018;16:5905–35.

[9] O'Reilly GJ, Perrone D, Fox M, Monteiro R, Filiatrault A. Seismic Assessment and Loss Estimation of Existing School Buildings in Italy. Eng Struct 2018;168:142–62.

[10] Foutch DA, Hjelmstad KD, Calderon EDV, Gutierrez EF, Downs RE. The Mexico earthquake of September 19, 1985: Case studies of seismic strengthening for two buildings in Mexico City. Earthquake Spectra 1989;5:153–74.

[11] Canbay E, Ersoy U, Ozcebe G. Contribution of reinforced concrete infills to seismic behavior of structural systems. ACI Struct J 2003;100:637–43.

[12] Seible F, Priestley MJN, Hegemier GA, Innamorato D. Seismic retrofit of RC columns with continuous carbon fiber jackets. Journal of Composites for Construction (ASCE) 1997;1(2):52–62.

[13] Triantafillou TC. Shear strengthening of reinforced concrete beams using epoxy-bonded FRP composites. ACI Struct J 1998;95(2):107–15.

[14] Binici B, Ozcebe G, Ozcelik R. Analysis and design of FRP composites for seismic retrofit of infill walls in reinforced concrete frames. Composite: Part B 2007;38:575–83.

[15] Ozcan O, Binici B, Ozcebe G. Improving seismic performance of deficient reinforced concrete columns using carbon fiber-reinforced polymers. Eng Struct 2008;30:1632–46.

[16] Tremblay R, Laxerte M, Christopoulos C. Seismic response of multistory buildings with self-centering energy dissipative steel braces. Journal of Structural Engineering ASCE 2008;134:108–20.

[17] Erochko J, Christopoulos C, Tremblay R, Kim HJ. Shake table testing and numerical simulation of a self-centering energy dissipative braced frame. Earthquake Eng Struct Dyn 2013;42:1617–35.

[18] Fan X, Xu LH, Li Z. Seismic performance evaluation of steel frames with pre-pressed spring self-centering braces. J Constr Steel Res 2019;162:105761.

[19] Xu LH, Fan X, Li Z. Seismic assessment of buildings with pre-pressed spring self-centering energy dissipation braces. Journal of Structural Engineering ASCE 2020;146:04019190.

[20] Qiu CX, Zhu S. Performance-based seismic design of self-centering steel frames with SMA-based braces. Eng Struct 2017;130:67–82.

[21] Badoux M, Jirsa JO. Steel bracing of RC frames for seismic retrofitting. J Struct Eng 1990;116:55–74.

[22] Fukuyama H, Sugano S. Japanese seismic rehabilitation of concrete buildings after the Hyogoken-Nanbu earthquake. Cem Concr Compos 2000;22:59–79.

[23] Ozcelik R, Binici B, Kurç O. Pseudo dynamic testing of an RC frame retrofitted with chevron braces. J Earthquake Eng 2012;16:515–39.

[24] Jara M, Hernandez C, Garcia R, Robles F. The Mexico earthquake of September 19, 1985: Typical cases of repair and strengthening of concrete buildings. Earthquake Spectra 1989;5:175–93.

[25] Jirsa JO. Divergent issues in rehabilitation of existing buildings. Earthquake Spectra 1994;10:95–112.

[26] Celik OC, Berman JW, Bruneau M. Cyclic Testing of Braces Laterally Restrained by Steel Studs. Journal of Structural Engineering ASCE 2005;131:1114–24.

[27] Broderick BM, Goggins J, Beg D, Elghazouli Ahmet Y, Mongabure P, Maoult AL, et al. Sinur F. Assessment of the seismic response of concentrically-braced steel frames. Experimental Research in Earthquake. Engineering 2015:327–44.

[28] O'Reilly GJ, Sullivan TJ. Probabilistic seismic assessment and retrofit considerations for Italian RC frame buildings. Bull Earthq Eng 2018;16:1447–85.

[29] Cardone D, Gesualdi G, Perrone G. Cost-Benefit Analysis of Alternative Retrofit Strategies for RC Frame Buildings. J Earthquake Eng 2019;23(2):208–41.

[30] Cardone D, Sullivan T, Gesualdi G, Perrone G. Simplified estimation of the expected annual loss of reinforced concrete buildings. Earthquake Eng Struct Dyn 2017;46:2009–32.

[31] Fujimoto M, Wada A, Saeki E, Takeuchi T, Watanabe A. Development of unbonded brace. Quarterly Column 1990;115:91–6.

[32] Takeuchi T. Buckling-Restrained Brace: History, Design and Applications. 9th International Conference on Behavior of Steel Structures in Seismic Areas 2018.

[33] Mahrenholtz1 C, Lin P.C, Wu A.C, Tsai K.C, Hwang J.H, Lin R.Y, Bhayusukma M.Y. Retrofit of reinforced concrete frames with buckling-restrained braces. Earthquake Engineering & Structural Dynamics 2015; 44: 59–78.

[34] Takeuchi T, Yasuda K, Iwata M. Seismic retrofitting using energy dissipation façade. ATC-SEI09 Conference on Improving the Seismic Performance of Buildings and Other Structures. San Francisco; 2009.

[35] Di Sarno L, Manfredi G. Seismic retrofitting with buckling restrained braces: Application to an existing non-ductile RC framed building. Soil Dyn Earthquake Eng 2010;30:1279–97.

[36] Chandra J, Warnitchai P. Application of Buckling Restrained Braces for Seismic Strengthening of Irregular Gravity Load Designed Reinforced Concrete Frame Buildings. Civil Engineering Dimension 2011;13:65–74.

[37] Di Sarno L, Manfredi G. Experimental tests on full-scale RC unretrofitted frame and retrofitted with buckling-restrained braces. Earthquake Eng Struct Dyn 2012;41:315–33.

[38] Habibi A, Chan RWK, Albermani F. Energy-based design method for seismic retrofitting with passive energy dissipation systems. Eng Struct 2013;46:77–86.

[39] Khampanit A, Leelataviwat A, Kochanin J, Warnitchai P. Energy-based seismic strengthening design of non-ductile reinforced concrete frames using buckling-restrained braces. Eng Struct 2014;81:110–22.

[40] Almeida A, Ferreira R, M.Proença J, Gago A.S, Seismic retrofit of RC building structures with Buckling Restrained Braces. Engineering Structures 2017; 130: 14–22.

[41] Fujishita K, Sutcu F, Matsui R, Takeuchi T. Damage distribution based energy-dissipation retrofit method for multi-story RC building in Turkey. IABSE Symposium Report 2015;104:1–8.

[42] Takeuchi T, Wada A. Buckling-restrained braces and application. The Japan Society of Seismic Isolation.

[43] Sutcu F, Takeuchi T, Matsui R. Seismic Retrofitting Design Method of Existing RC Buildings with Buckling Restrained Braces. J Constr Steel Res 2014;101:304–13.

[44] Sutcu F, Bal A, Fujishita K, Matsui R, Celik OC, Takeuchi T, et al. Experimental and Analytical Studies of Sub-Standard RC Frames Retrofitted with Buckling-Restrained Braces and Steel Frames. Bull Earthq Eng 2020;18:2389–410.

[45] Qu Z, Kishiki S, Maida Y, Sakata H, Wada A. Seismic responses of reinforced concrete frames with buckling restrained braces in zigzag configuration. Eng Struct 2015;105:12–21.

[46] Qu Z, Xie JJ, Wang T, Kishiki S. Cyclic loading test of double K-braced reinforced concrete frame subassemblies with buckling restrained braces. Engineering Structure 2017;139:1–14.

[47] Kasai K, Fu Y, Watanabe A. Passive Control Systems for Seismic Damage Mitigation. Journal of Structural Engineering ASCE 1998;124:501–12.

[48] Priestley MJN. Displacement-Based Seismic Assessment of Reinforced Concrete Buildings. J Earthquake Eng 1997;1:157–92.

[49] Jacobsen L. S. Damping in composite structures. 2nd World Conference on Earthquake Engineering 1960; 1029-1044.

[50] Kazantzi AK, Vamvatsikos D. The Hysteretic Energy as a Performance Measure in

Analytical Studies. Earthquake Spectra 2019;34:719–39.
[51] Newmark N.M, Rousenblueth E, Fundamentals of Earthquake Engineering. Prentice-Hall 555 Inc., 1971.
[52] Kasai K, Ito H, Ogura T. Passive Control Design Method Based on Tuning of Equivalent Stiffness of Bilinear Oil Damper. Journal of Structural and Construction Engineering 2008;73(630):1281–8.
[53] Takeda T, Sozen MA, Nielsen NN. Reinforced concrete response to simulated earthquakes. Journal of Structural Engineering ASCE (96) 1970;12:2557–73.
[54] The Building Center of Japan. The Building Standard Law of Japan on CD-ROM 2016.
[55] American Society of Civil Engineers (ASCE). Minimum Design Loads for Buildings and Other Structures 2016 (ASCE/SEI 7-16).
[56] Ferraioli M, Lavino A. A Displacement-Based Design Method for Seismic Retrofit of RC Buildings Using Dissipative Braces. Mathematical Problems in Engineering 2018;ID:5364564.
[57] Sullivan TJ, Saborio-Romano D, O'Reilly GJ, Welch DP, Landi L. Simplified Pushover Analysis of Moment Resisting Frame Structures. J Earthquake Eng 2018.
[58] Wilson EL. CSI Analysis Reference Manual For SAP 2000, ETABS, SAFE, and CSI Bridge. Berkeley: Computers & Structures, Inc; 2015.
[59] Mander JB, Priestley MJN. Park R. Theoretical Stress-Strain Model for Confined Concrete Journal of Structural Engineering ASCE 1988;114:1804–26.
[60] American Society of Civil Engineers (ASCE). Seismic Evaluation and Retrofit of Existing Buildings 2017 (ASCE/SEI 41-17).
[61] The Japan Building Disaster Prevention Association. Standard for Seismic Evaluation of Existing Reinforced concrete Buildings 2001.
[62] Department of Public Works and Town & Country Planning (DPT), Thailand Seismic Design Code 2009.
[63] Pacific Earthquake Engineering Research Center (PEER). PEER NGA Ground Motion Database, < https://ngawest2.berkeley.edu/site > .
[64] Yazgan U, Dazio A. Post-earthquake damage assessment using residual displacements. Earthquake Eng Struct Dyn 2012;41:1257–76.
[65] McCormick J, Aburano H, Ikenaga M, Nakashima M. Permissible Residual Deformation Levels for Building Structures Considering both Safety and Human Elements. 14th World Conference on Earthquake Engineering. 2008.